Passive imaging of moving targets exploiting multiple scattering using sparse distributed apertures

2012 Inverse Problems 28 125009

(http://iopscience.iop.org/0266-5611/28/12/125009)

Inverse Problems **28** (2012) 125009 (36pp) doi:10.1088/0266-5611/28/12/125009

Passive imaging of moving targets exploiting multiple scattering using sparse distributed apertures

Ling Wang[1] **and Birsen Yazıcı**[2]

[1] College of Electronic and Information Engineering, Nanjing University of Aeronautics and Astronautics, Nanjing, 210016, China
[2] Department of Electrical, Computer and Systems Engineering, Rensselaer Polytechnic Institute, Troy, NY 12180, USA

E-mail: yazici@ecse.rpi.edu

Received 10 November 2011, in final form 19 October 2012
Published 19 November 2012
Online at stacks.iop.org/IP/28/125009

Abstract

We present a new passive imaging method for moving targets using a sparse array of receivers and illumination sources of opportunity operating in multiple-scattering environments. We assume that the receivers are spatially distributed in an arbitrary fashion and the illumination sources of opportunity are non-cooperative where the locations of the transmitters and transmitted waveforms are unknown. Our method is capable of exploiting the multiple scattering in the environment. We use a physics-based and statistical approach to develop a model under Born approximation that relates the measurements at a given receiver to measurements at other receivers in terms of a hypothetical target in position and velocity spaces, the Green function of the background environment, as well as the statistics of the target, clutter and noise. Next, we use this model to formulate the imaging problem as a test of binary hypotheses for unknown target position and velocity, and address it by maximizing the signal-to-noise ratio of the test statistic. We use the resulting test statistic to form an image in position and velocity spaces. We illustrate our imaging method and analyze its resolution using a first-order specular reflection-based model of the Green function suitable for urban environments throughout the paper. We present numerical experiments to verify our theory and to demonstrate the performance of our method using practical waveforms of opportunity. While our primary interest is in radar imaging, our method can also be applied to passive acoustic and geophysical imaging.

(Some figures may appear in colour only in the online journal)

1. Introduction

With the rapid growth of broadcasting stations, mobile phone base stations, communication and navigation satellites, as well as relatively low cost and rapid deployment of receivers, passive imaging using transmitters of opportunity has emerged as an active area of research in recent years [1–24].

Passive imaging is of particular interest in urban areas due to the availability of a large number of transmitters of opportunity. Urban environments are also rich in multiple scattering. However, existing methods for passive imaging of moving targets implicitly assume a single-scattering environment. In this paper, we present a new passive imaging method for moving targets exploiting multiple scattering using a sparse array of receivers and non-cooperative transmitters of opportunity to reconstruct the distribution of targets in both position and velocity spaces. To the best of our knowledge, our paper presents the first passive moving target imaging method that exploits multiple scattering reported in the literature.

1.1. Related literature

Passive moving target detection and imaging have been studied by many researchers [1–20]. With the exception of [20], these works either assume *a priori* knowledge of the transmitter-related information or estimate this information from measurements. The works in [1–18] mainly focus on the detection of moving targets in a bi-static framework. In [19], a method is presented for imaging of airborne targets where a single receiver and multiple television transmitters are used. This method can be viewed as a multi-static inverse synthetic aperture radar imaging technique [25]. In [20], a passive detection technique for moving targets which exploits target thermal radiation was considered. This method is based on the cross-correlation of measurements from two different locations over a temporal window.

The technique of cross-correlation of measurements has also been used in passive synthetic aperture radar (SAR) imaging [23, 24] and other passive imaging applications [20, 22, 26–30]. The correlation processing eliminates the need for knowledge about the transmitter location and waveform. As a result, this approach is applicable to passive imaging using non-cooperative sources of opportunity. Our present work falls into this class of approaches.

In [23] and [24], we developed two correlation-based passive imaging methods combined with filtered-backprojection techniques to form high-resolution SAR images of ground radiance, which are suitable for wideband and ultra-narrowband illumination sources of opportunity, respectively. Both of these works address imaging of a stationary scene in free space. The delay-based correlation was also studied in [26–30] to image stationary heterogeneities in the context of geophysical imaging, where [27] considers random perturbations from the free-space Green function, resulting in a method based on windowed temporal correlations of measurements where the windowing function is determined based on the decoherence length and frequency of clutter.

In [22], we presented a passive imaging method using sparse distributed apertures in multiple-scattering environments. However, this method assumes that the targets are stationary during the transmission and reception and focuses on the reconstruction of targets in the position space only. This work as well as an earlier work by one of the authors introduces the hypothesis-testing-based approach to imaging [31]. In [32], we consider the problem of passive imaging of moving targets in free space using sparse distributed apertures to reconstruct the distribution of targets in both position and velocity spaces.

In [5–9], passive detection in multiple-scattering environments was considered. However, these studies treat multiple scattering as a part of clutter or interferences to be suppressed or removed. In [33–36], the target detection problem in multiple-scattering environments is considered. However, these studies are for an active imaging scenario where *a priori* knowledge about the transmitter locations and transmitted waveforms is available. In [33], the multipath components of the reflected signal are explored to improve the detection of stationary targets for the region of interest where the multipath components can be well separated. In [34], the potential of exploiting multiple scattering to improve dismount localization and classification

is pointed out based on experimental data analysis. In [35] and [36], the moving target detection problem in multiple scattering is studied using the OFDM waveforms. In [36], the multiple-scattering components of the received signal along with the sparse-signal recovery techniques are used to address the target detection problem.

1.2. Our approach and its advantages

We assume that a scene of interest with moving targets in a multiple-scattering environment is illuminated by non-cooperative transmitters of opportunity, and the field backscattered from the scene is measured by multiple receivers that are arbitrarily distributed around the scene of interest. We use a physics-based approach to model the incident and scattered fields from the multiple-scattering environment with moving targets. Assuming a hypothetical moving target, we develop a passive measurement model under Born approximation that relates the measurements at a given receiver to measurements at other receivers using the Green function of the environment as well as the statistics of the target, clutter and noise. We then use this model to formulate the imaging problem as a test of binary hypotheses to determine the presence of a moving target in position and velocity spaces. We address the resulting binary test of hypotheses within the framework of generalized likelihood ratio test (GLRT) and by maximizing the signal-to-noise ratio (SNR) of the test statistic. Our passive measurement model and the corresponding image formation method are applicable with an arbitrary Green's function. To illustrate the measurement model and the image formation explicitly, we use a Green's function model based on the first-order specular reflection suitable for urban-type multiple-scattering environments. We introduce the concepts of passive Doppler and passive range and show that the measurements at different receivers are related via passive Doppler and delay associated with the passive range along multiple-scattering paths. The resulting test statistic is the superposition of filtered, scaled and delayed correlations of measurements at different receivers. We analyze the resolution of the reconstructed images under different imaging scenarios including different number of receivers and transmitters and different types of transmitted waveforms. We compare the performance of our passive imaging method developed for multiple-scattering environments with our earlier work developed for free space [32]. Our analysis shows that the resolution of the position and velocity images improves due to the constructive contribution of the multiple scattering. However, artifacts also arise in the reconstructed images. We analyze the resolution and strength of the reconstructed target and artifacts. We present extensive numerical simulations to verify our theoretical analysis and to demonstrate the performance of our passive moving target imaging method using practical waveforms of opportunity. The results show the improvements in the resolution of the reconstructed images when the information about multiple scattering is exploited.

To the best of our knowledge, our method is the first in the literature that exploits multiple scattering for passive imaging of moving targets. Our method has the following advantages as compared to the existing passive imaging techniques. (1) Unlike the previous approaches [1–20, 32], we develop a passive measurement model and an associated image formation method that allows us to exploit multiple scattering in the environment for passive imaging of moving targets. Our method does not require any prior knowledge about the transmitter locations and transmitted waveforms. (2) As compared to the passive moving target imaging techniques in [1–19], our method does not require receivers with high directivity. (3) The GLRT-based image formation provides a framework to easily incorporate *a priori* information on targets, background clutter, as well as non-Gaussian data likelihood and prior models. (4) Our approach is applicable to both cooperative and non-cooperative transmitters of opportunity.

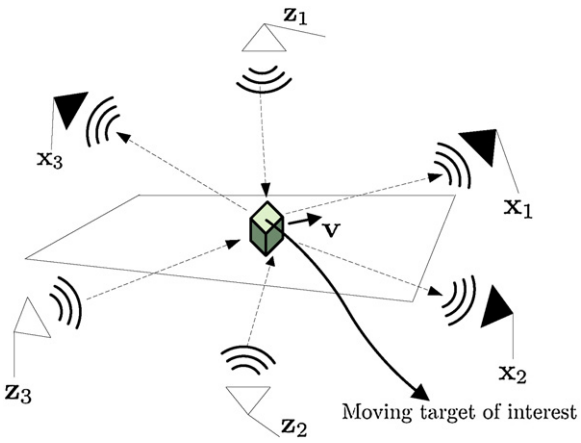

Figure 1. The figure illustrates a typical distributed aperture setup with receive and transmit antenna elements that are several hundred wavelengths apart. $\mathbf{x}_i,\ i = 1, \ldots, 3$ denote receivers and $\mathbf{z}_i,\ i = 1, \ldots, 3$ denote transmitters.

While our treatment focuses primarily on radar imaging, our method is also applicable to passive imaging of moving objects in seismic, acoustic and microwave imaging.

1.3. The organization of the paper

The rest of our paper is organized as follows. In section 2, we present the models for a moving target, incident field and scattered field, and develop a general passive measurement model applicable to arbitrary multiple-scattering environments. In section 3, we use a first-order specular reflection model for an urban-type multiple-scattering environment and present the corresponding explicit passive measurement model. In section 4, we address the moving target imaging problem within the GLRT framework using the passive measurement model developed in section 3. We also present an explicit formula for image formation based on the first-order specular reflection model of the Green function. In section 5, we present the resolution and SNR analysis of our method. In section 6, we present numerical simulations. Section 7 concludes our discussion.

2. Passive measurement model for the imaging of moving targets in multiple-scattering environments

We reserve $\mathbf{x}$ to denote location in 3D Euclidean space and $\boldsymbol{x}$ to denote location in 2D space. We denote operators ($\mathcal{P}, \mathcal{S}$, etc) with calligraphic letters. For a function f, $\hat{f}$ denotes its Fourier transform and f^* denotes its complex conjugate. Bold font denotes vector quantities. Non-bold italic font denotes scalar quantities.

2.1. Models for the moving targets, incident field and scattered field

We consider a sparse distribution of n receivers located at $\mathbf{x}_i,\ i = 1, \ldots, n$, and m transmitters located at $\mathbf{z}_q,\ i = 1, \ldots, m$, transmitting waveforms p_q starting at time $t = -T_{\mathbf{z}_q}$. The receivers and transmitters may be arbitrarily located with several hundred wavelengths apart with no assumption that transmitters and receivers are co-located. Figure 1 is an illustration of the distributed apertures. Non-identical waveforms may be transmitted from different transmitters.

We assume that the electromagnetic waves decay rapidly as they penetrate the ground [37]. We then write the three-dimensional moving target distribution $q_{\mathbf{v}}(\mathbf{x} - \mathbf{v}t)$ in terms of the two-dimensional location and two-dimensional velocity as follows:

$$q_{\mathbf{v}}(\mathbf{x} - \mathbf{v}t) = q_{\upsilon}(\boldsymbol{x} - \boldsymbol{\upsilon}t)\delta(x_3 - h(\boldsymbol{x}))\delta(\upsilon_3 - Dh(\boldsymbol{x}) \cdot \boldsymbol{\upsilon}), \tag{1}$$

where $q_{\mathbf{v}}(\mathbf{x})$ is the reflectivity function of the moving target at time $t = 0$ with $\mathbf{x} = (\boldsymbol{x}, x_3), \boldsymbol{x} \in \mathbb{R}^2$, and $\mathbf{v} = (\boldsymbol{\upsilon}, \upsilon_3), \boldsymbol{\upsilon} \in \mathbb{R}^2$, denotes the velocity associated with the location $\mathbf{x}$, $h : \mathbb{R}^2 \to \mathbb{R}$ represents the ground topography and $Dh(\boldsymbol{x}) = [\frac{\partial h}{\partial x_1} \quad \frac{\partial h}{\partial x_2}]$.

We consider a statistical target model to account for the scattering variations with the incident and scattering angles, as well as other factors, such as the frequency and polarization of electromagnetic waves, etc. We assume that $q_{\upsilon}(\mathbf{x})$ has finite-valued mean, $\bar{q}_{\upsilon}(\mathbf{x})$, and finite-valued covariance function, R^q. Furthermore, we assume that the target and clutter are mutually statistically uncorrelated.

Using the scalar wave equation, the measurement at the receiver located at $\mathbf{x}_i$, $i = 1, \ldots, N$ can be modeled as [22]

$$m_i(t) = \int g(\mathbf{x}_i, \boldsymbol{y} + \boldsymbol{\upsilon}\tau, t - \tau)q_{\upsilon}(\boldsymbol{y})\partial_\tau^2 E^{\text{tot}}(\boldsymbol{y} + \boldsymbol{\upsilon}\tau, \tau)\,\mathrm{d}\tau\,\mathrm{d}\boldsymbol{y}\,\mathrm{d}\upsilon + \tilde{n}_i(t), \tag{2}$$

where we define $g(\mathbf{x}, \boldsymbol{y}, t)$ as the 3D Green function of the background environment that is equal to $g(\mathbf{x}, (\boldsymbol{y}, h(\boldsymbol{y})), t)$ and E^{tot} denotes the total field given by

$$E^{\text{tot}} = E^{\text{sc}} + E^{\text{in}}, \tag{3}$$

where E^{sc} is the scattered field and E^{in} is the incident field given by

$$E^{\text{in}}(\boldsymbol{y} + \boldsymbol{\upsilon}\tau, \tau) = \sum_{q=1}^{M} \int g(\boldsymbol{y} + \boldsymbol{\upsilon}\tau, \mathbf{z}_q, \tau - \tau')p_q(\tau' + T_{\mathbf{z}_q})\,\mathrm{d}\tau'. \tag{4}$$

In (2), $\tilde{n}_i(t)$, $i = 1, \ldots, N$, denotes the measurements due to clutter[3] and additive thermal noise. Without loss of generality, we assume that $\tilde{n}_i(t)$, $i = 1, \cdots, N$, is zero-mean with autocovariance function $R_{\tilde{n}}$. Note that the isotropic antenna model is used in (4). However, this assumption is not necessary for the rest of our discussion and arbitrary antenna beampatterns can be easily incorporated into (4).

Note that in practical applications, the measured field could include not only the scattered field but also the so-called 'direct field', i.e. the incident field due to transmitters. This direct field, depending on the spatial configuration of the transmitters and receivers, can be relatively strong as compared to the field scattered from the target. In practical active imaging applications, the system has to be 'calibrated' to take into account not just the scattered field, but also the 'direct field'. The calibration of the system may require sophisticated analogue/experimental or signal processing methods [39]. A recent publication [40] has demonstrated using real data that the direct field contamination can be suppressed by designing a proper filter, where two co-located receivers having a direct line of sight to the transmitter as in [1–17] are used. For the rest of our discussion, we assume that the scattered field is available to image moving scatterers.

2.2. The forward- and back-propagation operators

Note that the measurement model in (2) and (4) is given in terms of the incident field, and hence the transmitted waveform and the transmitter location. However, for noncooperative passive detection and imaging applications, the information about the transmitted waveforms

[3] Note that in this work we define clutter not only as the reflected field from objects of no interest (non-target object) [38], but also from an unknown random object which deviates from a known deterministic background.

and the location of the transmitters may not be available. Thus, we develop an alternative measurement model that expresses the scattered field at each receiver in terms of the scattered field at a different receiver. This model is based on the fact that the measurements at all receiver are due to the same incident field E^{in}, target velocity $\boldsymbol{\upsilon}$ and the target distribution, $q_{\boldsymbol{\upsilon}}(\mathbf{y})$. The model involves back-propagating the measurement at a receiver location to a hypothetical target location moving with a hypothetical velocity and then forward propagating the resulting field to another receiver location.

We define the forward-propagation operator, $\mathcal{P}_{\mathbf{y},\boldsymbol{\upsilon},i}$, with respect to the ith receiver as follows:

$$\mathcal{P}_{\mathbf{y},\boldsymbol{\upsilon},i}[u](t) = \int W_s(\mathbf{y},\mathbf{y}')W_v(\boldsymbol{\upsilon},\boldsymbol{\upsilon}')g(\mathbf{x}_i,\mathbf{y}'+\boldsymbol{\upsilon}'\tau,t-\tau)u(\mathbf{y}',\boldsymbol{\upsilon}',\tau)\,\mathrm{d}\tau\,\mathrm{d}\mathbf{y}'\,\mathrm{d}\boldsymbol{\upsilon}', \tag{5}$$

where $u(\mathbf{y},\boldsymbol{\upsilon},\tau) = q_{\boldsymbol{\upsilon}}(\mathbf{y})\partial_\tau^2 E^{\text{tot}}(\mathbf{y}+\boldsymbol{\upsilon}\tau,\tau)$, $W_s(\mathbf{y}',\mathbf{y})$ is a spatial windowing function of unit amplitude centered at a hypothetical target location $\mathbf{y}$ at time $t=0$ and $W_v(\boldsymbol{\upsilon}',\boldsymbol{\upsilon})$ is a windowing function of unit amplitude in the velocity space centered at the hypothetical velocity $\boldsymbol{\upsilon}$. Note that the forward propagation operator is $\mathbf{y}$- and $\boldsymbol{\upsilon}$-dependent due to the windowing functions W_s and $W_{\boldsymbol{\upsilon}}$. These windowing functions can be chosen based on the support of the target centered at $\mathbf{y}$ and $\boldsymbol{\upsilon}$ in position and velocity spaces.

We define the back-propagation operator as the adjoint of $\mathcal{P}_{\mathbf{y},\boldsymbol{\upsilon},i}$ and denote it with $\mathcal{P}^*_{\mathbf{y},\boldsymbol{\upsilon},i}$ [41]. We can express the forward- and back-propagation operators respectively in the temporal Fourier transform space and define

$$\hat{\mathcal{P}}_{\mathbf{y},\boldsymbol{\upsilon},i} := \mathcal{F}\mathcal{P}_{\mathbf{y},\boldsymbol{\upsilon},i}\mathcal{F}^{-1}, \tag{6}$$

where $\mathcal{F}$ and $\mathcal{F}^{-1}$ denote the temporal Fourier transform and its inverse, respectively.

In an ideal scenario, where there is no clutter or noise in the measurements, we can express the ith measurement in terms of the jth measurement as follows:

$$\hat{m}_i^{(0)}(\omega) = \hat{\mathcal{P}}_{\mathbf{y},\boldsymbol{\upsilon},i}\hat{\mathcal{P}}^*_{\mathbf{y},\boldsymbol{\upsilon},j}\hat{m}_j^{(0)}(\omega), \tag{7}$$

where $\hat{m}_i^{(0)}(\omega)$ and $\hat{m}_j^{(0)}(\omega)$ are the Fourier transform of the clutter- and noise-free measurements at the ith and jth receivers, respectively. In the presence of clutter and noise, $\tilde{n}_j(t)$ is also back-propagated along with the noise- and clutter-free part of the received signal, $\hat{m}_j^{(0)}(\omega)$. Therefore, if we denote $\hat{m}_j = \hat{m}_j^{(0)} + \hat{\tilde{n}}_j$, where $\hat{\tilde{n}}_j(t)$ is the Fourier transform of $\tilde{n}_j(t)$, then the expression for the passive measurement model at the ith receiver in terms of the jth measurement becomes

$$\begin{aligned}\hat{m}_i(\omega) &= \hat{\mathcal{P}}_{\mathbf{y},\boldsymbol{\upsilon},i}\hat{\mathcal{P}}^*_{\mathbf{y},\boldsymbol{\upsilon},j}\hat{m}_j^{(0)}(\omega) + \hat{\mathcal{P}}_{\mathbf{y},\boldsymbol{\upsilon},i}\hat{\mathcal{P}}^*_{\mathbf{y},\boldsymbol{\upsilon},j}\hat{\tilde{n}}_j(t) + \hat{\tilde{n}}_i(t)\\ &= \hat{\mathcal{P}}_{\mathbf{y},\boldsymbol{\upsilon},i}\hat{\mathcal{P}}^*_{\mathbf{y},\boldsymbol{\upsilon},j}\hat{m}_j(\omega) + \hat{\tilde{n}}_i(\omega).\end{aligned} \tag{8}$$

Figure 2 illustrates the passive measurement model given by (8). As compared to the model that we defined for stationary targets [22], the velocity of the targets is incorporated into the forward and back-propagation operators, which allows us to estimate the velocities of the moving targets, in addition to their positions.

2.3. Vectorized passive measurement model for distributed apertures

We form a vector measurement model by taking one of the receivers as a reference. Without loss of generality, we take the jth receiver as a reference and form the following measurement vector:

$$\mathbf{m} = [\hat{m}_1 \quad \hat{m}_2 \quad \cdots \quad \hat{m}_N]^T. \tag{9}$$

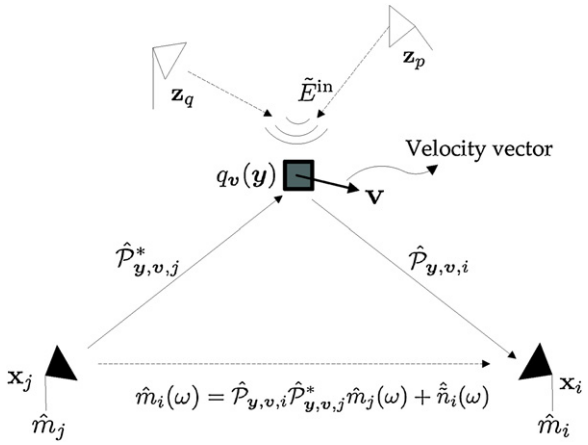

Figure 2. An illustration of the back-propagation of the scattered field at the jth receiver to a hypothetical target location moving with a hypothetical target velocity and forward-propagation of the resulting field to the ith receiver.

Similarly, we can vectorize the 'reference measurements' and the noise as follows:

$$\mathbf{m_r} = [\hat{m}_j \quad \hat{m}_j \quad \cdots \quad \hat{m}_j]^T \tag{10}$$

$$\mathbf{n} = [\hat{\tilde{n}}_1 \quad \hat{\tilde{n}}_2 \quad \cdots \quad \hat{\tilde{n}}_N]^T, \tag{11}$$

where $\hat{\tilde{n}}_i$, $i \neq j$ is measurement due to clutter plus additive thermal noise at the ith receiver. Note that $\mathbf{m}$, $\mathbf{m_r}$ and $\mathbf{n}$ are all $(N-1)$-dimensional vectors.

The composition of the back-propagation and forward-propagation operators can be represented as a diagonal matrix given by

$$\mathbf{P}_{\boldsymbol{y},\boldsymbol{v}} = \text{diag}\big[\hat{\mathcal{P}}_{\boldsymbol{y},\boldsymbol{v},1}\hat{\mathcal{P}}^*_{\boldsymbol{y},\boldsymbol{v},j} \quad \cdots \quad \hat{\mathcal{P}}_{\boldsymbol{y},\boldsymbol{v},N}\hat{\mathcal{P}}^*_{\boldsymbol{y},\boldsymbol{v},j}\big], \tag{12}$$

where $i \neq j$ and $\mathbf{P}_{\boldsymbol{y},\boldsymbol{v}}$ is $(N-1) \times (N-1)$.

Using (8)–(12), we form a vectorized passive measurement model as follows:

$$\mathbf{m}(\omega) = \mathbf{P}_{\boldsymbol{y},\boldsymbol{v}}\mathbf{m_r}(\omega) + \mathbf{n}(\omega) \tag{13}$$

for some range of ω. Note that in (13), all operations are understood to be elementwise.

Note that the passive measurement model derived in this section and the image formation method described in section 4 are applicable for an arbitrary multiple-scattering environment. In the following section, we focus on a specific Green's function model for the multiple-scattering environments and express the operators, $\mathcal{P}$, $\hat{\mathcal{P}}$, $\mathcal{P}^*$ and $\hat{\mathcal{P}}^*$ explicitly. This Green's function model results in an explicit passive measurement model and an explicit image formation formula described in the following two sections.

3. A multiple-scattering environment model based on specular reflections and the corresponding passive measurement model

3.1. A Green's function model for the multiple-scattering environments based on first-order specular reflections

For multiple-scattering environments, when the scatterers are well separated, the Green function of the background environment can be modeled in the following form:

$$\hat{g}(\mathbf{x}, \mathbf{y}, \omega) = \sum_{s \in \text{paths}} \tilde{a}_s(\mathbf{x}, \mathbf{y}, \omega)\, \mathrm{e}^{-\mathrm{i}\omega\tau_s(\mathbf{x},\mathbf{y})}, \tag{14}$$

where τ_s denotes the travel time along the path s and $\tilde{a}_s$ is an amplitude factor that depends on the geometric spreading factors and the strength of the scatterers. This model is known as the ray-theoretic Green function [42].

Experimental radar studies conducted in urban environments have shown that the multiple-scattering responses are primarily due to reflections from the specular region in the background environment, such as a wall or a light pole, etc [43]. Thus, we approximate (14) by considering only the paths originating from the target to a background scatterer and from the background scatterer to the receiver, i.e. the first-order specular reflections. For L scatterers embedded in a homogenous medium, this results in L multipath bounces between the target and the background medium. In this case, the model in (14) can be approximated by

$$\hat{g}(\mathbf{x}, \mathbf{y}, \omega) = \frac{\mathrm{e}^{-\mathrm{i}k|\mathbf{x}-\mathbf{y}|}}{4\pi|\mathbf{x}-\mathbf{y}|} + \sum_{l=1}^{L} a_l \frac{\mathrm{e}^{-\mathrm{i}k(|\mathbf{y}_l-\mathbf{y}|+|\mathbf{x}-\mathbf{y}_l|)}}{4\pi|\mathbf{y}_l-\mathbf{y}||\mathbf{x}-\mathbf{y}_l|}, \tag{15}$$

where each term represents a specular reflection from a background scatterer, $k = \omega/c_0$ is the wavenumber, c_0 denotes the speed of wave propagation in free space, $\mathbf{y}_l$, $l = 1, \ldots, L$ denotes the location of the lth scatterer and $a_l < 1$ is the corresponding attenuation coefficient. The Green function above is referred to as the shoot-and-bounce model [44]. See also the recent studies [45–47] that use the first-order specular reflection model with known attenuation coefficients to model multiple scattering in urban environments for radar applications.

We further assume that all multipath bounces are specular reflections. This allows us to model the environment as a collection of mirror planes. Each plane, $\mathcal{A}$, is characterized by its normal vector $\mathbf{a}$, and an affine plane equation given as

$$\mathcal{A} := \{\mathbf{x} : \mathbf{x} \cdot \mathbf{a} = d\}, \tag{16}$$

where d is a scalar that determines the location of the plane. This allows us to express the multipath components of the Green function given in (15) using the *mirror antenna elements* as follows:

$$\hat{g}(\mathbf{x}, \mathbf{y}, \omega) = \frac{\mathrm{e}^{-\mathrm{i}k|\mathbf{x}-\mathbf{y}|}}{4\pi|\mathbf{x}-\mathbf{y}|} + \sum_{l=1}^{L} a_l \frac{\mathrm{e}^{-\mathrm{i}k|\mathbf{x}^l-\mathbf{y}|}}{4\pi|\mathbf{x}^l-\mathbf{y}|} \tag{17}$$

$$= \sum_{l=0}^{L} a_l \frac{\mathrm{e}^{-\mathrm{i}k|\mathbf{x}^l-\mathbf{y}|}}{4\pi|\mathbf{x}^l-\mathbf{y}|}, \tag{18}$$

where

$$\mathbf{x}^l = \mathbf{x} - 2\frac{\mathbf{x}\cdot\mathbf{a}_l - d_l}{|\mathbf{a}_l|^2}\mathbf{a}_l, \quad l = 1, \ldots, L \quad \text{and} \quad a_0 = 1,\ \mathbf{x}^0 = \mathbf{x}\,. \tag{19}$$

Note that $\mathbf{x}^l$, the *mirror receiver* location, is the reflection of $\mathbf{x}$ about the plane, $\mathcal{A}_l$ defined by the normal $\mathbf{a}_l$ and the scalar d_l associated with the lth, $l = 1, \ldots, L$ multipath bounce, a_l is the corresponding attenuation coefficient and $\mathbf{x}^0$ is the location of the receiver. Figure 3 illustrates the concept of mirror receivers in two-dimensional space.

We can express (18) as

$$\hat{g}(\mathbf{x}, \mathbf{y}, \omega) = \sum_{l=0}^{L} a_l \hat{g}_0(\mathbf{x}^l, \mathbf{y}, \omega), \tag{20}$$

where $\hat{g}_0(\mathbf{x}^l, \mathbf{y}, \omega)$ denotes the temporal Fourier transform of the free-space *Green function* given by

$$\hat{g}_0(\mathbf{x}^l, \mathbf{y}, \omega) = \frac{\mathrm{e}^{-\mathrm{i}k|\mathbf{x}^l-\mathbf{y}|}}{4\pi|\mathbf{x}^l-\mathbf{y}|}\,. \tag{21}$$

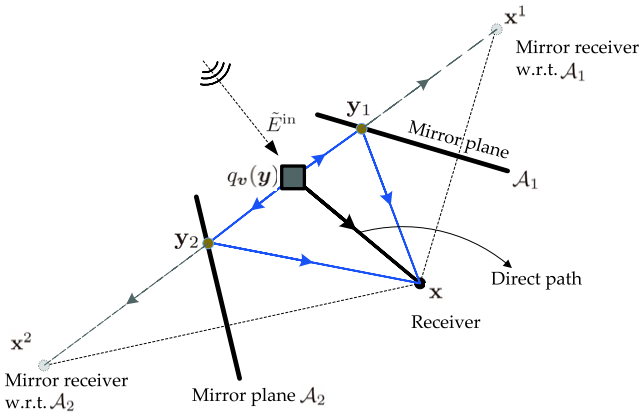

Figure 3. An illustration of the mirror receivers in 2D space. $\mathbf{x}$ denotes the receiver location. $\mathbf{x}^l$, $l = 1, 2$ denote the mirror receivers with respect to the mirror planes $\mathcal{A}_l$, $l = 1, 2$, respectively. $\mathbf{y}_1$ and $\mathbf{y}_2$ denote the location of the scatterers associated with each mirror plane. $q_{\boldsymbol{v}}(\boldsymbol{y})$ denotes the target. The solid blue lines indicate the multipath wave propagation.

Note that practical experiments have shown that the multipath responses are primarily due to reflections from the specular region in the background environment, such as a wall, as well as other structures such as a light pole, metal downpour, etc [34]. Therefore, the shoot-and-bounce model described above is considered sufficient to capture the multiple scattering in urban areas [35, 36, 47].

3.2. Passive measurement model for moving targets using the first-order specular reflection model

We assume that the moving targets are slow movers, i.e. the speed of the target, $|\boldsymbol{v}|$, is much smaller than the speed of light or $|\boldsymbol{v}|t$ is much less than the distance between the receiver (transmitter) and the target. Using the Taylor series expansions of $|\mathbf{x}_i^l - (\mathbf{y} + \mathbf{v}\tau)|$ and $|\mathbf{y} + \mathbf{v}\tau - \mathbf{z}_q^\nu|$ at $\tau = 0$ and making the approximations up to the first order, we have

$$g_0(\mathbf{x}_i^l, \boldsymbol{y} + \boldsymbol{v}\tau, t - \tau) \approx g_0\left(\mathbf{x}_i^l, \boldsymbol{y}, t - \left(1 - \frac{\widehat{\mathbf{x}_i^l - \mathbf{y}} \cdot \mathbf{v}}{c_0}\right)\tau\right), \tag{22}$$

$$g_0(\mathbf{y} + \boldsymbol{v}\tau, \mathbf{z}_q^\nu, \tau - \tau') \approx g_0\left(\boldsymbol{y}, \mathbf{z}_q^\nu, \left(1 - \frac{\widehat{\mathbf{y} - \mathbf{z}_q^\nu} \cdot \mathbf{v}}{c_0}\right)\tau - \tau'\right), \tag{23}$$

where g_0 is the time-domain free-space Green function

$$g_0(\mathbf{x}, \mathbf{y}, t) = \frac{\delta(t - |\mathbf{x} - \mathbf{y}|/c_0)}{4\pi|\mathbf{x} - \mathbf{y}|}, \tag{24}$$

$\mathbf{z}_q^0 = \mathbf{z}_q$, $\mathbf{z}_q^\nu$, $\nu = 1, \ldots, L$ denote the locations of the *mirror transmitters*, i.e. the reflections of the transmitters located at $\mathbf{z}_q$ about the plane $\mathcal{A}_\nu$; and $\mathbf{x}_i^0 = \mathbf{x}_i$, $\mathbf{x}_i^l$, $l = 1, \ldots, L$ denote the locations of the mirror receivers. Note that $\mathbf{y} = (\boldsymbol{y}, h(\boldsymbol{y}), t)$ and $\mathbf{v} = (\boldsymbol{v}, Dh(\boldsymbol{y}) \cdot \boldsymbol{v})$.

Substituting the Green function of the multipath environment given by the inverse Fourier transform of (20) into (2) and using (22) and (23), we obtain

$$m_i(t) = \sum_{l=0}^{L} a_l \int g_0(\mathbf{x}_i^l, \mathbf{y}, t - \mu_{\mathbf{y},\boldsymbol{v},\mathbf{x}_i^l}\tau) q_{\boldsymbol{v}}(\boldsymbol{y}) \partial_\tau^2 \tilde{E}^{\text{in}}(\mathbf{y}, \tau)\, \mathrm{d}\tau\, \mathrm{d}\mathbf{y}\, \mathrm{d}\boldsymbol{v} + \tilde{n}_i(t), \tag{25}$$

where $\tilde{E}^{\text{in}}$ denotes the incident filed observed by the moving target given by

$$\tilde{E}^{\text{in}}(\boldsymbol{y},\tau)=\sum_{q=1}^{M}\left(\sum_{\nu=0}^{L}\int g_0(\boldsymbol{y},\mathbf{z}_q^{\nu},\tilde{\mu}_{\boldsymbol{y},\boldsymbol{\upsilon},\mathbf{z}_q^{\nu}}\tau-\tau')p_q(\tau'+T_{\mathbf{z}_q^{\nu}})\,\mathrm{d}\tau'\right) \tag{26}$$

and the scale factors $\mu_{\boldsymbol{y},\boldsymbol{\upsilon},\mathbf{x}_i^l}$ and $\tilde{\mu}_{\boldsymbol{y},\boldsymbol{\upsilon},\mathbf{z}_q^{\nu}}$ are given as follows:

$$\mu_{\boldsymbol{y},\boldsymbol{\upsilon},\mathbf{x}_i^l}=1+\widehat{\mathbf{y}-\mathbf{x}_i^l}\cdot\mathbf{v}/c_0, \tag{27}$$

$$\tilde{\mu}_{\boldsymbol{y},\boldsymbol{\upsilon},\mathbf{z}_q^{\nu}}=1-\widehat{\mathbf{y}-\mathbf{z}_q^{\nu}}\cdot\mathbf{v}/c_0\,. \tag{28}$$

We refer to $\mu_{\boldsymbol{y},\boldsymbol{\upsilon},\mathbf{x}_i^l}$ as the *multipath Doppler-scale factor observed at location* $\mathbf{x}$ *due to a moving target* with velocity $\boldsymbol{\upsilon}$ at location $\boldsymbol{y}$ associated with the lth multipath propagation and $\tilde{\mu}_{\boldsymbol{y},\boldsymbol{\upsilon},\mathbf{z}_q^{\nu}}$ as the *multipath Doppler-scale factor observed by the moving target* located at $\boldsymbol{y}$ moving with velocity $\boldsymbol{\upsilon}$ due to a waveform transmitted from $\mathbf{z}_q$ along the νth multipath bounce.

Equation (25) shows that the measurement at the receiver consists of the reflected signals due to the direct-path propagation corresponding to $l=0$ and multiple multipath propagations corresponding to $l\neq 0$.

Using (5) and the Fourier transform of (20), the forward-propagation operator in temporal Fourier domain becomes

$$\hat{\mathcal{P}}_{\boldsymbol{y},\boldsymbol{\upsilon},i}[\hat{u}](\omega)=\sum_{l=0}^{L}a_l\int W_s(\boldsymbol{y},\boldsymbol{y}')W_v(\boldsymbol{\upsilon},\boldsymbol{\upsilon}')\hat{g}_0(\mathbf{x}_i^l,\boldsymbol{y}',\omega)\hat{u}(\boldsymbol{y}',\boldsymbol{\upsilon}',\mu_{\boldsymbol{y}',\boldsymbol{\upsilon}',\mathbf{x}_i^l}\omega)\,\mathrm{d}\boldsymbol{y}'\,\mathrm{d}\boldsymbol{\upsilon}', \tag{29}$$

where $\hat{u}$ is the temporal Fourier transform of $u(\boldsymbol{y},\boldsymbol{\upsilon},\tau)=q_{\upsilon}(\boldsymbol{y})\partial_{\tau}^2\tilde{E}^{\text{in}}(\boldsymbol{y},\tau)$.

Assuming that the moving target is composed of a collection of point targets in position and velocity spaces, we decompose $\hat{\mathcal{P}}_{\boldsymbol{y},\boldsymbol{\upsilon},i}$ in (29) as follows:

$$\hat{\mathcal{P}}_{\boldsymbol{y},\boldsymbol{\upsilon},i}[\hat{u}](\omega)=\sum_{l=0}^{L}a_l\mathcal{G}_{\boldsymbol{y},i}^l\mathcal{S}_{\boldsymbol{\upsilon},i}^l[u](\omega), \tag{30}$$

where

$$\mathcal{S}_{\boldsymbol{\upsilon},i}^l[\hat{u}](\omega)=\mu_{\boldsymbol{y},\boldsymbol{\upsilon},\mathbf{x}_i^l}\,\hat{u}(\boldsymbol{y},\boldsymbol{\upsilon},\mu_{\boldsymbol{y},\boldsymbol{\upsilon},\mathbf{x}_i^l}\,\omega), \tag{31}$$

$$\mathcal{G}_{\boldsymbol{y},i}^l[\hat{u}](\omega)=\frac{\hat{u}(\boldsymbol{y},\boldsymbol{\upsilon},\omega)\mathrm{e}^{-\mathrm{i}k|\mathbf{x}_i^l-\boldsymbol{y}|}}{4\pi|\mathbf{x}_i^l-\boldsymbol{y}|}\quad\text{for}\quad l=0,\ldots,L. \tag{32}$$

Note that $\hat{u}$ is viewed as a function of ω only, and $\boldsymbol{y}$ and $\boldsymbol{\upsilon}$ are fixed parameters.

In (31), $\mathcal{S}_{\boldsymbol{\upsilon},i}^l$, $l=0,\ldots,L$, is the scaling operator that accounts for the Doppler effect observed by the ith receiver due to a moving target with velocity $\boldsymbol{\upsilon}$ at location $\boldsymbol{y}$ associated with the lth, $l=1,\ldots,L$, multipath bounce and the direct path corresponding to $l=0$. In (32), $\mathcal{G}_{\boldsymbol{y},i}^l$, $l=0,\ldots,L$, is the operator that accounts for the wave propagation in the stationary background from the target to the ith receiver via the lth, $l=1,\ldots,L$, multipath bounce and the direct path corresponding to $l=0$ and a_l is the corresponding attenuation coefficient.

We approximate the back-propagation operator $\hat{\mathcal{P}}_{\boldsymbol{y},\boldsymbol{\upsilon},i}^{-1}$ using the adjoints of $\mathcal{S}_{\boldsymbol{\upsilon},i}^l$ and $\mathcal{G}_{\boldsymbol{y},i}^l$ as follows:

$$\hat{\mathcal{P}}_{\boldsymbol{y},\boldsymbol{\upsilon},i}^{-1}\approx\hat{\mathcal{P}}_{\boldsymbol{y},\boldsymbol{\upsilon},i}^{*}=\sum_{l=0}^{L}a_l^*\mathcal{S}_{\boldsymbol{\upsilon},i}^{l,*}\mathcal{G}_{\boldsymbol{y},i}^{l,*}, \tag{33}$$

where

$$\mathcal{S}_{\boldsymbol{\upsilon},i}^{l,*}[\hat{m}](\omega)=\hat{m}_i\left(\frac{\omega}{\mu_{\boldsymbol{y},\boldsymbol{\upsilon},\mathbf{x}_i^l}}\right), \tag{34}$$

$$\mathcal{G}_{\boldsymbol{y},i}^{l,*}[\hat{m}](\omega)=\frac{\hat{m}_i(\omega)\,\mathrm{e}^{\mathrm{i}k|\mathbf{x}_i^l-\boldsymbol{y}|}}{4\pi|\mathbf{x}_i^l-\boldsymbol{y}|},\quad\text{for}\quad l=0,\ldots,L\,. \tag{35}$$

3.3. Passive measurement model for a moving point target

We model a moving point target as follows:

$$q_{\boldsymbol{v}}(\boldsymbol{y}) = \rho\,\delta(\boldsymbol{y}-\boldsymbol{y}_0)\delta(\boldsymbol{v}-\boldsymbol{v}_0), \tag{36}$$

where ρ is the reflectivity of the point target located at $\boldsymbol{y}_0$, at time $t=0$, $\boldsymbol{v}_0$ is the velocity of the moving target. For the target model in (36), the forward-propagating operator in (30) reduces to

$$\hat{\mathcal{P}}_{\boldsymbol{y}_0,\boldsymbol{v}_0,i}[u](\omega) = \sum_{l=0}^{L} a_l \hat{g}_0(\mathbf{x}_i^l, \boldsymbol{y}_0, \omega)\mu_{\boldsymbol{y}_0,\boldsymbol{v}_0,\mathbf{x}_i^l}\hat{u}(\mu_{\boldsymbol{y}_0,\boldsymbol{v}_0,\mathbf{x}_i^l}, \omega)\,. \tag{37}$$

The back-propagation operator in (33) becomes

$$\hat{\mathcal{P}}^*_{\boldsymbol{y}_0,\boldsymbol{v}_0,i}[\hat{m}_i](\omega) = \sum_{l=0}^{L} a_l^* \hat{m}_i\left(\frac{\omega}{\mu_{\boldsymbol{y}_0,\boldsymbol{v}_0,\mathbf{x}_i^l}}\right)\hat{g}_0^*\left(\mathbf{x}_i^l, \boldsymbol{y}_0, \frac{\omega}{\mu_{\boldsymbol{y}_0,\boldsymbol{v}_0,\mathbf{x}_i^l}}\right)\,. \tag{38}$$

Using (8), (37), (38) and (21), we obtain

$$\hat{m}_i(\omega) = \sum_{l,p=0}^{L} \frac{a_l a_p^* \mu_{\boldsymbol{y}_0,\boldsymbol{v}_0,\mathbf{x}_i^l}}{(4\pi)^2|\mathbf{x}_j^p-\mathbf{y}_0||\mathbf{x}_i^l-\mathbf{y}_0|}\exp\big[-\mathrm{i}kR_{ij}^{\beta}(\mathbf{y}_0,\mathbf{v}_0)\big]\hat{m}_j\big(\gamma_{\boldsymbol{y}_0,\boldsymbol{v}_0}^{ij,\beta}\,\omega\big) + \hat{\tilde{n}}_i(\omega)\,. \tag{39}$$

In (39) $\gamma_{\boldsymbol{y}_0,\boldsymbol{v}_0}^{ij,\beta}$, $\beta=(l,p)$, is the ratio of the Doppler-scale factors between the target and the ith and jth receivers along the lth and pth multipath bounces which is given by

$$\gamma_{\boldsymbol{y}_0,\boldsymbol{v}_0}^{ij,\beta} := \frac{\mu_{\boldsymbol{y}_0,\boldsymbol{v}_0,\mathbf{x}_i^l}}{\mu_{\boldsymbol{y}_0,\boldsymbol{v}_0,\mathbf{x}_j^p}} = \frac{1+\widehat{\mathbf{y}_0-\mathbf{x}_i^l}\cdot\mathbf{v}_0/c_0}{1+\widehat{\mathbf{y}_0-\mathbf{x}_j^p}\cdot\mathbf{v}_0/c_0} \qquad \beta=(l,p). \tag{40}$$

We refer to $\gamma_{\boldsymbol{y}_0,\boldsymbol{v}_0}^{ij,\beta}$, $\beta=(l,p)$, as the *passive-Doppler-scale factor* due to a moving target with velocity $\mathbf{v}_0$ with respect to the ith and jth receivers along the lth, pth multipath bounces.

In (39), $R_{ij}^{\beta}(\mathbf{y}_0,\mathbf{v}_0)$ is the range difference of the ith and jth receivers to the target located at $\mathbf{y}_0$ moving with velocity $\mathbf{v}_0$ along the l^{th}, pth multipath bounces. This range is given by

$$R_{ij}^{\beta}(\mathbf{y}_0,\mathbf{v}_0) := |\mathbf{x}_i^l-\mathbf{y}_0| - \gamma_{\boldsymbol{y}_0,\boldsymbol{v}_0}^{ij,\beta}|\mathbf{x}_j^p-\mathbf{y}_0|. \tag{41}$$

We refer to $R_{ij}^{\beta}(\mathbf{y}_0,\mathbf{v}_0)$ as the *passive range for moving targets* due to the velocity of the target $\mathbf{v}_0$ and the range difference between the ith and jth receivers along the lth, pth multi-bounces.

Note that in (39), (40) and (41), $\mathbf{y}_0=(\boldsymbol{y}_0,h(\boldsymbol{y}_0))$ and $\mathbf{v}_0=(\boldsymbol{v}_0,Dh(\boldsymbol{y}_0)\cdot\boldsymbol{v}_0)$.

Equation (39) shows that the measurement at the ith receiver can be expressed as a superposition of the scaled and delayed version of the measurement at the jth receiver over all possible paths including the direct and multi-bounce paths. The scale factor is given by $\gamma_{\boldsymbol{y}_0,\boldsymbol{v}_0}^{ij,\beta}$ and the delay is given by $(|\mathbf{x}_i^l-\mathbf{y}_0|-\gamma_{\boldsymbol{y}_0,\boldsymbol{v}_0}^{ij,\beta}|\mathbf{x}_j^p-\mathbf{y}_0|)/c_0$ for each path.

4. Image formation

In this section, we first describe the image formation method for the passive measurement model given for an arbitrary multiple-scattering environment introduced in section 2, and next describe the imaging method for the passive measurement model derived based on first-order specular reflection model of the multiple-scattering environment introduced in section 3.

4.1. Image formation using the arbitrary Green function model of the multiple-scattering environment

We use a hypothesis testing based approach to address the passive imaging problem which has its root in the generalized likelihood ratio test (GLRT) [48]. We set up a position- and velocity-resolved binary hypotheses testing and next determine a test statistic for each location $(\boldsymbol{y}, h(\boldsymbol{y})) \in \mathbb{R}^3$ and each velocity $(\boldsymbol{v}, Dh(\boldsymbol{y}) \cdot \boldsymbol{v}) \in \mathbb{R}^3$ in the position and velocity spaces using the passive measurement model for moving targets developed in section 2. The image is then formed in the $(\boldsymbol{y}, \boldsymbol{v})$ domain with the position- and velocity-resolved test statistic. Recall that the clutter and noise are zero-mean with finite variance and covariance functions and the target reflectivity function is assumed to be random to account for the variation with the angle of incidence and scattering.

We consider the following test of binary hypothesis for each location and velocity in $(\boldsymbol{y}, \boldsymbol{v})$ space:

$$\begin{aligned} \mathcal{H}_0 :&\quad \mathbf{m} = \mathbf{n} \\ \mathcal{H}_1 :&\quad \mathbf{m} = \mathbf{P}_{\boldsymbol{y},\boldsymbol{v}}\mathbf{m}_{\mathbf{r}} + \mathbf{n}, \end{aligned} \tag{42}$$

where $\mathbf{P}_{\boldsymbol{y},\boldsymbol{v}}$, $\mathbf{m}_{\mathbf{r}}$, $\mathbf{m}$ and $\mathbf{n}$ are as defined in (9)–(13).

The null hypothesis states that the measurement is due to clutter and noise, whereas the alternative hypothesis states that the measurement is due to a target located at $\boldsymbol{y}$ moving with velocity $\boldsymbol{v}$.

We design the following linear discriminant functional to address the binary hypothesis testing problem,

$$\lambda = \langle \mathbf{m}, \mathbf{w} \rangle := \int \mathbf{w}^H \mathbf{m} \, \mathrm{d}\omega = \sum_{i,i\neq j} \int w_i^*(\omega) \hat{m}_i(\omega) \, \mathrm{d}\omega, \tag{43}$$

where λ denotes the output of the discriminant functional, which we call the *test statistic*, and $\mathbf{w}$ is a template given by

$$\mathbf{w} = [w_1 \quad w_2 \quad \cdots \quad w_N]^T. \tag{44}$$

We determine the test statistic by maximizing the SNR of λ. The expression for the SNR of λ for processes with finite first- and second-order statistics is given as [48]

$$\mathrm{SNR}_\lambda = \frac{|\mathrm{E}\,[\lambda|\mathcal{H}_1] - \mathrm{E}\,[\lambda|\mathcal{H}_0]\,|}{\sqrt{1/2(\mathrm{Var}[\lambda|\mathcal{H}_1] + \mathrm{Var}[\lambda|\mathcal{H}_0])}}, \tag{45}$$

where E denotes the expectation operator and Var denotes the variance operator.

The optimal linear template maximizing (45) is given by [22, 32]

$$\mathbf{w}_{\mathrm{opt}} = \overline{\mathcal{R}}^{-1} \mathbf{P}_{\boldsymbol{y},\boldsymbol{v}} \overline{\mathbf{m}}_{\mathbf{r}}, \tag{46}$$

where $\mathcal{R}$ is a symmetric non-negative definite integral operator with the matrix kernel $\overline{\mathbf{R}} = 1/2[\mathbf{P}_{\boldsymbol{y},\boldsymbol{v}}(\mathbf{R}_q + \mathbf{R}_{\mathbf{n}_{\mathbf{r}}})\mathbf{P}_{\boldsymbol{y},\boldsymbol{v}}^H + 2\mathbf{R}_{\mathbf{n}}]$. $\mathbf{R}_q$ is the autocovariance of the clutter- and noise-free reference measurements in the presence of a statistical target given by

$$\mathbf{R}_q(\omega, \omega') = \mathrm{E}\left[(\mathbf{m}_{\mathbf{r}}^{(0)}(\omega) - \bar{\mathbf{m}}_{\mathbf{r}}(\omega))(\mathbf{m}_{\mathbf{r}}^{(0)}(\omega') - \bar{\mathbf{m}}_{\mathbf{r}}(\omega'))^H\right], \tag{47}$$

where $\mathbf{m}_{\mathbf{r}}^{(0)}(\omega) = [\hat{m}_j^{(0)}, \hat{m}_j^{(0)}, \cdots, \hat{m}_j^{(0)}]$ and $\bar{\mathbf{m}}_{\mathbf{r}}(\omega) = \mathrm{E}[\hat{m}_j(\omega)]$. $\mathbf{R}_{\mathbf{n}}$ is the autocovariance of the measurements due to clutter and noise, i.e. $\mathbf{R}_{\mathbf{n}}(\omega, \omega') = \mathrm{E}[\mathbf{n}(\omega)\mathbf{n}^H(\omega')]$ and $\mathbf{R}_{\mathbf{n}_{\mathbf{r}}}$ is the autocovariance of the reference measurements due to clutter and noise, $\mathbf{n}_j := [\hat{\hat{n}}_j, \hat{\hat{n}}_j, \cdots, \hat{\hat{n}}_j]$, i.e. $\mathbf{R}_{\mathbf{n}_{\mathbf{r}}}(\omega, \omega') = \mathrm{E}\left[\mathbf{n}_{\mathbf{r}}(\omega)\mathbf{n}_{\mathbf{r}}^H(\omega')\right]$. Note that $\mathbf{R}_q$, $\mathbf{R}_{\mathbf{n}}$ and $\mathbf{R}_{\mathbf{n}_{\mathbf{r}}}$ can be position and velocity dependent. (46) shows that the optimal template is position and velocity dependent.

For deterministic moving targets, where $\mathbf{R}_q = 0$, under the assumption that the measurements due to clutter and noise at different receivers are wide sense stationary and mutually uncorrelated, the resulting optimal linear template reduces to

$$\mathbf{w}_{\text{opt}} = \overline{\mathbf{S}}^{-1}\mathbf{P}_{y,\upsilon}\overline{\mathbf{m}}_{\mathbf{r}}, \tag{48}$$

where $\overline{\mathbf{S}}^{-1}$ is the inverse of $\overline{\mathbf{S}}$ defined by

$$\overline{\mathbf{S}}(\omega) = \int \overline{\mathbf{R}}(\omega, \omega')\,\mathrm{d}\omega'. \tag{49}$$

Note that the integration in (49) should be understood elementwise. We can show that $\overline{\mathbf{S}}^{-1}$ can be approximated by a diagonal matrix [32]. We denote diagonal elements of $\overline{\mathbf{S}}^{-1}$ by $\overline{S}_i^{-1}(\omega)$, $i = 1, \ldots, N$ and $i \neq j$, which is a function of the power spectral density function of measurements due to clutter and noise at the ith receiver and the kernel of $\mathbf{P}_{y,\upsilon}$.

4.2. Image formation using the first-order specular reflection model of the multiple-scattering environment

In this subsection, we combine the results derived in the previous subsection with the passive measurement model derived for the multiple-scattering environment based on the first-order specular reflections introduced in section 3. Plugging (39) into (48), each component of the optimal template becomes

$$w_i = \sum_{l,p=0}^{L} \frac{a_l a_p^* \mu_{\mathbf{y},\upsilon,\mathbf{x}_i^l}}{(4\pi)^2 |\mathbf{x}_j^p - \mathbf{y}||\mathbf{x}_i^l - \mathbf{y}|} \overline{S}_i^{-1}(\omega) \exp\left[-\mathrm{i}kR_{ij}^{\beta}(\mathbf{y}, \mathbf{v})\right] \mathrm{E}\left[\hat{m}_j\left(\gamma_{\mathbf{y},\upsilon}^{ij,\beta}\,\omega\right)\right], \tag{50}$$

where $i = 1, \ldots, N$ and $i \neq j$ and $\gamma_{\mathbf{y},\upsilon}^{ij,\beta}$, $\beta = (l, p)$, is the passive-Doppler-scale factor defined in (40) and $R_{ij}^{\beta}(\mathbf{y}, \mathbf{v})$ is the passive delay for a target located at $\mathbf{y}$ moving with velocity $\mathbf{v}$ as defined in (41). It is given by

$$R_{ij}^{\beta}(\mathbf{y}, \mathbf{v}) = |\mathbf{x}_i^l - \mathbf{y}| - \gamma_{\mathbf{y},\upsilon}^{ij,\beta}|\mathbf{x}_j^p - \mathbf{y}|. \tag{51}$$

In (50), the first term involves scaling due to geometrical spreading factors, a Doppler-scale factor and the attenuation coefficients associated with the multipath propagation. The second term is a pre-whitening filter due to colored clutter and noise. The third term involves passive delay due to the range difference of the two receivers to the moving target. The last term involves averaged dilated reference measurement. Note that the range difference in the exponential term considers all the possible propagation paths between the ith and jth receivers, including the range difference between the direct-paths, multipath bounces and the direct-path back-propagation and lth, $l = 1, \ldots, L$, multipath forward propagation and vice versa between the two receivers.

Plugging (50) into (43), we obtain the output of the linear discriminant functional $\lambda(\boldsymbol{y}, \boldsymbol{\upsilon})$ or the pixel value at $(\boldsymbol{y}, \boldsymbol{\upsilon})$ given by

$$\lambda(\boldsymbol{y}, \boldsymbol{\upsilon}) = \sum_{i,i\neq j}^{N} \sum_{l,p=0}^{L} \int \frac{a_l a_p^* \mu_{\mathbf{y},\upsilon,\mathbf{x}_i^l}}{(4\pi)^2 |\mathbf{x}_j^p - \mathbf{y}||\mathbf{x}_i^l - \mathbf{y}|} \mathrm{E} \times \left[m_j'\left(\frac{t - |\mathbf{y} - \mathbf{x}_i^l|/c_0}{\gamma_{\mathbf{y},\upsilon}^{ij,\beta}} + \frac{|\mathbf{y} - \mathbf{x}_j^p|}{c_0} \right) \right] m_i^*(t)\,\mathrm{d}t, \tag{52}$$

where $m_j'(t)$ is the filtered version of $m_j(t)$ with the filtering determined by $\overline{S}_i^{-1}(\omega)$. Equation (52) can be viewed as a superposition of the correlations between the filtered,

delayed, scaled (or dilated) replica of the reference measurement m_j and the measurement m_i, $i \neq j$.

Note that for the free-space Green function, l, $p = 0$ and $\mathbf{x}_i^0 = \mathbf{x}_i$, $\mathbf{x}_j^0 = \mathbf{x}_j$. Thus, (52) reduces to the test-statistic obtained for the passive imaging of moving targets in free space presented in [32].

5. Resolution analysis

In this section, we analyze the resolution of our imaging method using the first-order specular reflection model of the multiple-scattering environment. We focus our analysis on a deterministic moving point target model and analyze how moving targets in the multiple-scattering environment are resolved in the four-dimensional image $\lambda(\boldsymbol{y}, \boldsymbol{\upsilon}), \boldsymbol{y}, \boldsymbol{\upsilon} \in \mathbb{R}^2$. We analyze the resolution in terms of the point spread function (PSF) and the SNR of the position- and velocity-resolved test-statistic image.

We first present the PSF of the imaging operator for a general scenario involving N receivers, M transmitters and L scatterers in the background. Next, we use this PSF and analyze the resolution for a simple scenario involving two receivers and one transmitter to distill the important aspects of our analysis. We, then, extend our results to the case of multiple pairs of receivers and multiple transmitters. Finally, we present the SNR_λ^2 of the four-dimensional image to demonstrate the effect of multipath propagation and the number of antenna elements in the image contrast.

5.1. The PSF of the imaging operator

The PSF, $K(\boldsymbol{y}, \boldsymbol{y}_0; \boldsymbol{\upsilon}, \boldsymbol{\upsilon}_0)$, of the imaging operator is the image of a moving point target represented by the Dirac-delta function in position and velocity spaces, i.e. $\delta(\boldsymbol{y}-\boldsymbol{y}_0)\delta(\boldsymbol{\upsilon}-\boldsymbol{\upsilon}_0)$, with $\boldsymbol{y}$ serving as the spatial index of the image and $\boldsymbol{y}_0$ as the location of the point target at time $t = 0$, $\boldsymbol{\upsilon}$ serving as the velocity index of the image, and $\boldsymbol{\upsilon}_0$ as the velocity of the point target. Since the test statistic is a random variable, the expected value of the position- and velocity-resolved test statistic can be interpreted as the PSF, i.e. $K(\boldsymbol{y}, \boldsymbol{y}_0; \boldsymbol{\upsilon}, \boldsymbol{\upsilon}_0) := \mathrm{E}[\lambda(\boldsymbol{y}, \boldsymbol{\upsilon})]$.

The SNR of $\lambda(\boldsymbol{y}, \boldsymbol{\upsilon})$ as defined in (45) can be interpreted as the *contrast-to-noise ratio* of the resulting image [49].

Without loss of generality, we assume that the surface topography is flat, i.e. $h(\boldsymbol{y}) = h$, for some $\boldsymbol{y} \in \mathbb{R}^2$ and set $\mathbf{y} = [\boldsymbol{y}, h]$, $\mathbf{v} = [\boldsymbol{\upsilon}, 0]$. We take the measurement at the jth receiver as the reference. For a moving point target model given in (36), performing the Fourier transform of (25) and (26) and using (21), we obtain

$$\mathrm{E}\left[\hat{m}_j(\omega)\right] = \sum_{p,\nu=0}^{L} \sum_{q=1}^{M} C_{p,\nu}^{j} \omega^2 \exp\left[\mathrm{i}\Phi\left(\omega, \mathbf{x}_j^p, \mathbf{z}_q^\nu\right)\right] \hat{p}_q\left(\frac{\omega}{\alpha_{p,\nu}^{j,q}}\right), \tag{53}$$

where

$$\Phi(\omega, \mathbf{x}_j^p, \mathbf{z}_q^\nu) = \frac{\omega}{\alpha_{p,\nu}^{j,q}}\left[T_{\mathbf{z}_q} - \frac{|\mathbf{y}_0 - \mathbf{z}_q^\nu|}{c_0}\right] - \omega\frac{|\mathbf{y}_0 - \mathbf{x}_j^p|}{c_0}, \tag{54}$$

$$\alpha_{p,\nu}^{j,q} = \frac{\tilde{\mu}_{\mathbf{y}_0,\boldsymbol{\upsilon}_0,\mathbf{z}_q^\nu}}{\mu_{\mathbf{y}_0,\boldsymbol{\upsilon}_0,\mathbf{x}_j^p}} = \frac{1 - \widehat{\mathbf{y}_0 - \mathbf{z}_q^\nu} \cdot \mathbf{v}_0/c_0}{1 + \widehat{\mathbf{y}_0 - \mathbf{x}_j^p} \cdot \mathbf{v}_0/c_0}, \tag{55}$$

and $C_{p,\nu}^{j,q}$ is given by

$$C_{p,\nu}^{j,q} = \frac{-a_p a_\nu \rho}{(4\pi)^2 |\mathbf{y}_0 - \mathbf{x}_j^p||\mathbf{y}_0 - \mathbf{z}_q^\nu|(\alpha_{p,\nu}^{j,q})^3}. \tag{56}$$

Note that $\alpha_{p,\nu}^{j,q}$ and $C_{p,\nu}^{j,q}$ are both $\mathbf{y}_0$ and $\mathbf{v}_0$ dependent. We suppress this dependence to simplify our notation.

Thus, using (43) and (50), we obtain

$$K(\mathbf{y},\mathbf{y}_0;\boldsymbol{\upsilon},\boldsymbol{\upsilon}_0)=\sum_{q,q'=1}^{M}\sum_{i=1,i\neq j}^{N}\sum_{\kappa,\kappa'=0}^{L}C_{\kappa,\kappa'}^{ij,q,q'}\int S_i^{-1}(\omega)\omega^4\exp\left[-\mathrm{i}k\Delta_{ij}(\mathbf{y},\mathbf{y}_0;\beta;\beta')\right]$$
$$\times\exp\left[-\mathrm{i}k\Psi_{ij,q,q'}(\omega,\mathbf{y},\mathbf{v};\mathbf{y}_0,\mathbf{v}_0;\kappa,\kappa')\right]\hat{p}_{q'}\left(\frac{\gamma_{\mathbf{y},\boldsymbol{\upsilon}}^{ij,\beta}\omega}{\alpha_{p',\nu'}^{j,q'}}\right)\hat{p}_q^*\left(\frac{\omega}{\alpha_{l',\nu}^{i,q}}\right)\mathrm{d}\omega, \tag{57}$$

where κ and κ' are multi-indices defined as $\kappa=(\beta,\nu)$ and $\kappa'=(\beta',\nu')$ with $\beta=(l,p)$. $\gamma_{\mathbf{y},\boldsymbol{\upsilon}}^{ij,\beta}$ is the passive-Doppler-scale factor defined in (40), and $\Delta_{ij}(\mathbf{y},\mathbf{y}_0;\beta;\beta')$ is the difference of the passive-range terms defined as

$$\Delta_{ij}(\mathbf{y},\mathbf{y}_0;\beta;\beta')=\underbrace{(|\mathbf{y}-\mathbf{x}_i^l|-\gamma_{\mathbf{y},\boldsymbol{\upsilon}}^{ij,\beta}|\mathbf{y}-\mathbf{x}_j^p|)}_{R_{ij}^{\beta}(\mathbf{y},\mathbf{v})}-(|\mathbf{y}_0-\mathbf{x}_i^{l'}|-\gamma_{\mathbf{y},\boldsymbol{\upsilon}}^{ij,\beta}|\mathbf{y}_0-\mathbf{x}_j^{p'}|)\,. \tag{58}$$

The function $\Psi_{ij,q,q'}$ in (57) is given by

$$\Psi_{ij,q,q'}(\omega,\mathbf{y},\mathbf{v};\mathbf{y}_0,\mathbf{v}_0;\kappa,\kappa')=\frac{\gamma_{\mathbf{y},\boldsymbol{\upsilon}}^{ij,\beta}}{\alpha_{p',\nu'}^{j,q'}}\left(T_{\mathbf{z}_{q'}}c_0-|\mathbf{y}_0-\mathbf{z}_{q'}^{\nu'}|\right)-\frac{1}{\alpha_{l',\nu}^{i,q}}\left(T_{\mathbf{z}_q}c_0-|\mathbf{y}_0-\mathbf{z}_q^{\nu}|\right). \tag{59}$$

$\Psi_{ij,q,q'}$ is the difference of the ranges of the qth and q'th transmitter along the νth and ν'th multi-bounces to the target located at $\mathbf{y}_0$ moving with velocity $\mathbf{v}_0$.

From the resolution analysis point of view the most important terms in the PSF function above are those that involve the Doppler scaling factors in the third line and the phase term involving the difference of the passive ranges, $\Delta_{ij}(\mathbf{y},\mathbf{y}_0;\beta;\beta')$, and the term $\Psi_{ij,q,q'}$. The constant term $C_{\kappa,\kappa'}^{ij,q,q'}$ does not affect the resolution and is given by

$$C_{\kappa,\kappa'}^{ij,q,q'}=\frac{a_l a_p^*(\gamma_{\mathbf{y},\boldsymbol{\upsilon}}^{ij,\beta})^2\mu_{\mathbf{y},\boldsymbol{\upsilon},\mathbf{x}_i^l}}{(4\pi)2|\mathbf{x}_j^p-\mathbf{y}||\mathbf{x}_i^l-\mathbf{y}|}C_{l',\nu}^{i,q}C_{p',\nu'}^{j,q'}. \tag{60}$$

Intuitively speaking, for the resolution analysis, we want to determine where the PSF peaks in the image $(\boldsymbol{y},\boldsymbol{\upsilon})$ when the target is located at $\boldsymbol{y}_0$ moving with velocity $\boldsymbol{\upsilon}_0$, and the spread of the PSF, as well as its SNR at the peak value. These are analyzed for different scenarios in the following three subsections.

5.2. Resolution analysis for two receivers and a single transmitter

We assume that there are only two receivers located at $\mathbf{x}_1$ and $\mathbf{x}_2$ and a single transmitter located at $\mathbf{z}_1$. We take the measurement at the first receiver as the reference. Thus, the PSF in (57) reduces to

$$K(\mathbf{y},\mathbf{y}_0;\boldsymbol{\upsilon},\boldsymbol{\upsilon}_0)=\sum_{\kappa,\kappa'=0}^{L}C_{\kappa,\kappa'}^{21,1,1}\int S_2^{-1}(\omega)\omega^4\exp\left[-\mathrm{i}k\Delta_{21}(\mathbf{y},\mathbf{y}_0;\beta,\beta')\right]$$
$$\times\exp\left[\mathrm{i}k\Psi_{21,1,1}(\omega,\mathbf{y},\mathbf{y}_0;\mathbf{v},\mathbf{v}_0;\kappa,\kappa')\right]\hat{p}_1\left(\frac{\gamma_{\mathbf{y},\boldsymbol{\upsilon}}^{21,\beta}\omega}{\alpha_{p',\nu'}^{1,1}}\right)\hat{p}_1^*\left(\frac{\omega}{\alpha_{l',\nu}^{2,1}}\right)\mathrm{d}\omega, \tag{61}$$

where κ and κ' are as described above, Δ_{21}, $\Psi_{21,1,1}$, $\alpha_{p',\nu'}^{1,1}$, $\alpha_{l',\nu}^{2,1}$ and $C_{\kappa,\kappa'}^{21,1,1}$ are given by (58), (59), (55) and (60) for $i=2$, $j=1$ and $q=q'=1$, respectively. Note that each coefficient $C_{\kappa,\kappa'}^{21,1,1}$ and the summand in (61) are non-negative. Thus, $K(\boldsymbol{y},\boldsymbol{y}_0;\boldsymbol{\upsilon},\boldsymbol{\upsilon}_0)$ is maximized if each summand is maximized.

Examining (61), we see that if

$$\frac{\gamma_{\mathbf{y},\boldsymbol{\upsilon}}^{21,\beta}}{\alpha_{p',\nu'}^{1,1}} = \frac{1}{\alpha_{l',\nu}^{2,1}}, \quad \text{for all} \quad \kappa, \kappa', \tag{62}$$

then (61) becomes

$$\begin{aligned} K(\mathbf{y}, \mathbf{y}_0; \boldsymbol{\upsilon}, \boldsymbol{\upsilon}_0) = \sum_{\kappa,\kappa'=0}^{L} C_{\kappa,\kappa'}^{21,1,1} \int S_2^{-1}(\omega)\omega^4 \\ \times \exp\left[-\mathrm{i}k\left(\Delta_{21}(\mathbf{y}, \mathbf{y}_0; \beta, \beta') - \frac{\gamma_{\mathbf{y},\boldsymbol{\upsilon}}^{21,\beta}}{\alpha_{p',\nu'}^{1,1}}(|\mathbf{y}_0 - \mathbf{z}_1^{\nu}| - |\mathbf{y}_0 - \mathbf{z}_1^{\nu'}|)\right)\right] \\ \times \left|\hat{p}_1\left(\frac{\omega}{\alpha_{l',\nu}^{2,1}}\right)\right|^2 \mathrm{d}\omega\,. \end{aligned} \tag{63}$$

Equation (63) can be interpreted as a generalized auto-ambiguity function of the transmitted waveform p_1 [38]. Clearly, (63) attains its maximum whenever

$$\Delta_{21}(\mathbf{y}, \mathbf{y}_0; \beta, \beta') - \frac{\gamma_{\mathbf{y},\boldsymbol{\upsilon}}^{21,\beta}}{\alpha_{p',\nu'}^{1,1}}\big(|\mathbf{y}_0 - \mathbf{z}_1^{\nu}| - |\mathbf{y}_0 - \mathbf{z}_1^{\nu'}|\big) = 0 \quad \text{for all} \quad \kappa, \kappa'. \tag{64}$$

Thus, the PSF of the imaging operator for the two receivers and a single transmitter case becomes maximum whenever the two conditions given in (62) and (64) are satisfied. To identify the points $(\mathbf{y}, \boldsymbol{\upsilon})$ where the image attains its maximum, we define two types of manifolds based on (62) and (64).

Let

$$F_{21}^{\beta}(C) = \{(\mathbf{y}, \boldsymbol{\upsilon}) \in \mathbb{R}^2 \times \mathbb{R}^2 : \gamma_{\mathbf{y},\boldsymbol{\upsilon}}^{21,\beta} = C\} \tag{65}$$

for some constant $C \in \mathbb{R}^+$ and $\beta = (l, p)$. We refer to $F_{21}^{\beta}(C)$, i.e. those points $(\mathbf{y}, \boldsymbol{\upsilon}) \in \mathbb{R}^2 \times \mathbb{R}^2$ for which the passive-Doppler-scale factor $\gamma_{\mathbf{y},\boldsymbol{\upsilon}}^{21,\beta}$ observed by a pair of receivers along the lth and pth multi-path bounces is constant as the *passive-iso-Doppler manifold*.

Note that $\gamma_{\mathbf{y},\boldsymbol{\upsilon}}^{21,\beta} = C$ can be approximately expressed as

$$(\widehat{\mathbf{y} - \mathbf{x}_2^{l}} - \widehat{\mathbf{y} - \mathbf{x}_1^{p}}) \cdot \mathbf{v} = (C - 1)c_0, \quad l, p = 0, \ldots, L, \tag{66}$$

for slow-moving targets.

Thus, (62) specifies multiple passive-iso-Doppler manifolds each one corresponding to a pair of real or mirror receivers and real or mirror transmitters, i.e.

$$\gamma_{\mathbf{y},\boldsymbol{\upsilon}}^{21,\beta} = \frac{\alpha_{p',\nu'}^{1,1}}{\alpha_{l',\nu}^{2,1}} = \frac{1 + \widehat{\mathbf{y}_0 - \mathbf{x}_2^{l'}} \cdot \mathbf{v}_0/c_0}{1 + \widehat{\mathbf{y}_0 - \mathbf{x}_1^{p'}} \cdot \mathbf{v}_0/c_0} \cdot \frac{1 - \widehat{\mathbf{y}_0 - \mathbf{z}_1^{\nu'}} \cdot \mathbf{v}_0/c_0}{1 - \widehat{\mathbf{y}_0 - \mathbf{z}_1^{\nu}} \cdot \mathbf{v}_0/c_0}, \quad \text{for all} \quad \kappa, \kappa' \tag{67}$$

with $\kappa, \kappa' = (\beta, \nu) = (l, p, \nu)$.

Similarly, let

$$H_{21}^{\beta}(C) = \{(\mathbf{y}, \boldsymbol{\upsilon}) \in \mathbb{R}^2 \times \mathbb{R}^2 : R_{21}^{\beta}(\mathbf{y}, \mathbf{v}) = C\}, \tag{68}$$

where $R_{21}^{\beta}(\mathbf{y}, \mathbf{v})$ is the passive range given by (51) for $i = 2$ and $j = 1$, and $C \in \mathbb{R}^+$ is a constant and $\beta = (l, p)$. We refer to $H_{21}^{\beta}(C)$, i.e. those points $(\mathbf{y}, \boldsymbol{\upsilon}) \in \mathbb{R}^2 \times \mathbb{R}^2$ for which the passive range of a pair of receivers is constant as the *passive-iso-range manifold*.

Thus, using (58), (64) specifies multiple passive-iso-range manifolds each one corresponding to a pair of real or mirror receivers, i.e.

$$R_{21}^{\beta}(\mathbf{y}, \mathbf{v}) = |\mathbf{y}_0 - \mathbf{x}_2^{l'}| - \gamma_{\mathbf{y},\boldsymbol{\upsilon}}^{21,\beta}|\mathbf{y}_0 - \mathbf{x}_1^{p'}| + \frac{\gamma_{\mathbf{y},\boldsymbol{\upsilon}}^{21,\beta}}{\alpha_{p',\nu'}^{1,1}}\big(|\mathbf{y}_0 - \mathbf{z}_1^{\nu}| - |\mathbf{y}_0 - \mathbf{z}_1^{\nu'}|\big) \tag{69}$$

for all κ, κ' with $\kappa, \kappa' = (\beta, \nu) = (l, p, \nu)$.

Note that as compared to the free-space case [32], additional passive-iso-Doppler manifolds and passive-iso-range manifolds arise due to the multipath propagation in the environment.

We see that the PSF peaks at the intersection of multiple passive-iso-Doppler manifolds given in (67), and multiple passive-iso-range manifolds given in (69). The resolution of the reconstructed image in $(\boldsymbol{y}, \boldsymbol{v})$ is determined by the overlapping region between the passive-iso-Doppler and passive-iso-range manifolds. The size of this region depends on the spread of the passive-iso-Doppler and passive-iso-range manifolds determined by the shape of the generalized auto-ambiguity function defined by (63). The cross-section of the overlapping region for a constant velocity determines the position resolution, while the cross-section of the overlapping region for a constant position determines the velocity resolution.

More specifically, the position resolution is related to the spread of the cross-section of the passive-iso-Doppler manifold for a constant velocity, which we refer to as the *position-related passive-iso-Doppler contour*, and the spread of the cross-section of the passive-iso-range manifold for a constant velocity, which we refer to as the *position-related passive-iso-range contour*, depending on the range and Doppler ambiguities of the transmitted waveform: if the transmitted waveform has good Doppler resolution, but poor range resolution, then the position resolution primarily depends on the spread of the position-related passive-iso-Doppler contours. If, on the other hand, the transmitted waveform has only good range resolution, then the position reconstruction primarily depends on the spread of the position-related passive-iso-range contours. Note that if the transmitted waveform has both good Doppler and good range resolution, then the position resolution depends on the cross-section of the intersection of the passive-iso-Doppler and passive-iso-range manifolds for a constant velocity, which is neither the position-related passive-iso-Doppler contour nor the position-related passive-iso-range contour. However, this cross-section becomes one of two types of the contours described above as the range or Doppler resolution of the waveform degrades, or as the Doppler or range resolution improves.

The velocity resolution, on the other hand, is related to the spread of the cross-section of the passive-iso-Doppler manifold for a constant position depending on the Doppler ambiguity of the transmitted waveform. We refer to this cross-section as the *velocity-related passive-iso-Doppler contour*. Note that it can be shown that the *velocity-related passive-iso-range contour*, i.e. the cross-section of the passive-iso-range manifold for a constant position is the same as the *velocity-related passive-iso-Doppler contour*.

Note that for $\kappa = \kappa'$, (67) and (69) become

$$\gamma_{\boldsymbol{y},\boldsymbol{v}}^{21,\beta} = \frac{1 + \widehat{\mathbf{y}_0 - \mathbf{x}_2^l} \cdot \mathbf{v}_0/c_0}{1 + \widehat{\mathbf{y}_0 - \mathbf{x}_1^p} \cdot \mathbf{v}_0/c_0} = \gamma_{\mathbf{y}_0,\boldsymbol{v}_0}^{21,\beta} \tag{70}$$

and

$$R_{21}^{\beta}(\mathbf{y}, \mathbf{v}) = R_{21}^{\beta}(\mathbf{y}_0, \mathbf{v}_0), \tag{71}$$

respectively. Equations (70) and (71) show that the multiple passive-iso-Doppler and passive-iso-range manifolds for $\kappa = \kappa'$ ($l = l'$, $p = p'$ and $\nu = \nu'$) intersect at the correct target location and correct target velocity, which contribute to the true target image reconstruction in $(\boldsymbol{y}, \boldsymbol{v})$ space. As compared to the imaging in free space [32], the test-statistic value at the correct target location and correct target velocity increases by roughly a factor of $(L+1)^3$, where L is the number of multipath bounces.

However, as can be seen in (67) and (69), the passive-iso-Doppler manifolds and passive-iso-range manifolds corresponding to $\kappa \neq \kappa'$ ($l \neq l'$, or $p \neq p'$, or $\nu \neq \nu'$) do not intersect at the correct target location, $\boldsymbol{y}_0$, and correct target velocity, $\boldsymbol{v}_0$, which may lead to artifacts in the

reconstructed image. In subsection 5.4, we present the SNR of the target and artifacts which is associated with the strength of the reconstructed target and artifacts.

5.3. Resolution analysis for multiple pairs of receivers and multiple transmitters

We express (57) as

$$\begin{aligned} K(\mathbf{y},\mathbf{y}_0;\boldsymbol{\upsilon},\boldsymbol{\upsilon}_0) = & \sum_{q=q'=1}^{M}\sum_{i=1,i\neq j}^{N}\sum_{\kappa=\kappa'=0}^{L} C_{\kappa,\kappa}^{ij,q,q}\int S_i^{-1}(\omega)\omega^4 \exp\left[-\mathrm{i}k\Delta_{ij}(\mathbf{y},\mathbf{y}_0;\beta,\beta)\right] \\ & \times \exp\left[\mathrm{i}k\Psi_{ij,q,q}(\omega,\mathbf{y},\mathbf{y}_0;\mathbf{v},\mathbf{v}_0;\kappa,\kappa)\right]\hat{p}_q\left(\frac{\gamma_{\mathbf{y},\boldsymbol{\upsilon}}^{ij,\beta}\omega}{\alpha_{p,\nu}^{j,q}}\right)\hat{p}_q^*\left(\frac{\omega}{\alpha_{l,\nu}^{i,q}}\right)\mathrm{d}\omega \\ & + \sum_{q\neq q'}^{M}\sum_{i=1,i\neq j}^{N}\sum_{\kappa\neq\kappa'}^{L} C_{\kappa,\kappa'}^{ij,q,q'}\int S_i^{-1}(\omega)\omega^4 \exp\left[-\mathrm{i}k\Delta_{ij}(\mathbf{y},\mathbf{y}_0;\beta,\beta')\right] \\ & \times \exp\left[\mathrm{i}k\Psi_{ij,q,q'}(\omega,\mathbf{y},\mathbf{y}_0;\mathbf{v},\mathbf{v}_0;\kappa,\kappa')\right]\hat{p}_{q'}\left(\frac{\gamma_{\mathbf{y},\boldsymbol{\upsilon}}^{ij,\beta}\omega}{\alpha_{p',\nu'}^{j,q'}}\right)\hat{p}_q^*\left(\frac{\omega}{\alpha_{l',\nu}^{i,q}}\right)\mathrm{d}\omega, \quad (72) \end{aligned}$$

where Δ_{ij} and Ψ are given by (58) and (59), respectively.

Note that the first summation in (72) corresponding to $q = q'$, $\kappa = \kappa'$ contributes to the reconstruction of the true target image, while the second summation corresponding to $q \neq q'$ or $\kappa \neq \kappa'$ contributes to the reconstruction of the artifact components in the image.

As shown in the first summation in (72), for multiple pair receivers and multiple transmitters, there are multiple passive-iso-Doppler manifolds defined by

$$\frac{\gamma_{\mathbf{y},\boldsymbol{\upsilon}}^{ij,\beta}}{\alpha_{p,\nu}^{j,q}} = \frac{1}{\alpha_{l,\nu}^{i,q}} \Rightarrow \gamma_{\mathbf{y},\boldsymbol{\upsilon}}^{ij,\beta} = \gamma_{\mathbf{y}_0,\boldsymbol{\upsilon}_0}^{ij,\beta} \quad (73)$$

for $q = 1,\ldots,M$, $\kappa = 0,\ldots,L$ and $i \neq j$, $i = 1,\ldots,N$, and multiple passive-iso-range manifolds defined by

$$\Delta_{ij}^m(\mathbf{y},\mathbf{y}_0;\beta,\beta) = 0, \quad (74)$$

for $i \neq j, i = 1,\ldots,N$, $\beta = 0,\ldots,L$ intersecting at the correct target position and correct velocity in $(\mathbf{y},\boldsymbol{\upsilon})$ space. As a result the PSF increases roughly by a factor of $M(N-1)$ as compared to the two-receiver and a single-transmitter scenario described in subsection 5.2.

As can be seen in the second summation in (72), even for a single transmitter, multiple passive-iso-Doppler and passive-iso-range manifolds corresponding to $\kappa \neq \kappa'$, ($l \neq l'$ or $p \neq p'$ or $\nu \neq \nu'$) and $i = 1,\ldots,N$, $i \neq j$ do not intersect at the correct target position and correct target velocity in $(\mathbf{y},\boldsymbol{\upsilon})$ space and lead to additional artifacts in the reconstructed image as compared to the two-receiver, single transmitter case. These additional artifacts occur at the intersection of the passive-iso-Doppler manifolds defined by

$$\frac{\gamma_{\mathbf{y},\boldsymbol{\upsilon}}^{ij,\beta}}{\alpha_{p',\nu'}^{j,q'}} = \frac{1}{\alpha_{l',\nu}^{i,q}} \quad (75)$$

and the passive-iso-range manifolds defined by

$$R_{ij}^{\beta}(\mathbf{y},\mathbf{v}) = |\mathbf{y}_0 - \mathbf{x}_i^{l'}| - \gamma_{\mathbf{y},\boldsymbol{\upsilon}}^{ij,\beta}|\mathbf{y}_0 - \mathbf{x}_j^{p'}| + \frac{\gamma_{\mathbf{y},\boldsymbol{\upsilon}}^{ij,\beta}}{\alpha_{p',\nu'}^{j,q'}}\left(|\mathbf{y}_0 - \mathbf{z}_q^{\nu}| - |\mathbf{y}_0 - \mathbf{z}_{q'}^{\nu'}|\right) \quad (76)$$

for $q \neq q'$ and $\kappa,\kappa' = 0,\ldots,L$, $i \neq j, i = 1,\ldots,N$ may intersect at $\mathbf{y} \neq \mathbf{y}_0$ and $\boldsymbol{\upsilon} \neq \boldsymbol{\upsilon}_0$. However, the strength of these artifacts may be weak unless the waveforms transmitted from each transmitter correlate with each other well at arbitrary delays and scaling factors. However, this is an unlikely scenario for transmitters of opportunity.

5.4. SNR *of the reconstructed images*

The effect of multipath propagation, as well as using multiple pairs of receivers and multiple transmitters can also be observed in the SNR of the reconstructed image.

Using (12), (43), (45) and (53), we obtain the SNR_λ^2 at each location of the four-dimensional image:

$$\begin{aligned}\mathrm{SNR}_\lambda^2 = &\sum_{q=1}^{M}\sum_{i\neq j}^{N} C_{0,0}^{ij,q,q}\int \overline{S}_i^{-1}(\omega)\omega^4\left|\hat{p}_q\left(\frac{\gamma_{\mathbf{y},\boldsymbol{\upsilon}}^{ij,0}\,\omega}{\alpha_{0,0}^{j,q}}\right)\right|^2 \mathrm{d}\omega\\ &+\sum_{q=1}^{M}\sum_{i\neq j}^{N}\sum_{\kappa\neq 0,\kappa=\kappa'}^{L} C_{\Gamma,\Gamma}^{ij,q,q}\int \overline{S}_i^{-1}(\omega)\omega^4\left|\hat{p}_q\left(\frac{\gamma_{\mathbf{y},\boldsymbol{\upsilon}}^{ij,\beta}\,\omega}{\alpha_{p,\nu}^{j,q}}\right)\right|^2 \mathrm{d}\omega\\ &+\sum_{q\neq q'}^{M}\sum_{i\neq j}^{N}\sum_{\Gamma\neq\Gamma'}^{L} 2C_{\Gamma,\Gamma'}^{ij,q,q'}\,\mathrm{Re}\left[\int \overline{S}_i^{-1}(\omega)\omega^4\right.\\ &\times\exp\left[\mathrm{i}\left(\gamma_{\mathbf{y},\boldsymbol{\upsilon}}^{ij,\beta}\Phi\left(\omega,\mathbf{x}_j^{p''},\mathbf{z}_q^{\nu}\right)-\gamma_{\mathbf{y},\boldsymbol{\upsilon}}^{ij,\beta'}\Phi\left(\omega,\mathbf{x}_j^{p'''},\mathbf{z}_{q'}^{\nu'}\right)\right)\right]\\ &\left.\times\exp\left[-\mathrm{i}k(R_{ij}^{\beta}(\mathbf{y},\mathbf{v})-R_{ij}^{\beta'}(\mathbf{y},\mathbf{v}))\right]\hat{p}_q\left(\frac{\gamma_{\mathbf{y},\boldsymbol{\upsilon}}^{ij,\beta}\,\omega}{\alpha_{p'',\nu}^{j,q}}\right)\hat{p}_{q'}^{*}\left(\frac{\gamma_{\mathbf{y},\boldsymbol{\upsilon}}^{ij,\beta'}\,\omega}{\alpha_{p''',\nu'}^{j,q'}}\right)\mathrm{d}\omega\right], \qquad (77)\end{aligned}$$

where Γ and Γ' are multi-indices defined by $\Gamma=(l,p,p'',\nu)$ and $\Gamma=(l',p',p''',\nu')$,

$$C_{\Gamma,\Gamma'}^{ij,q,q'}=\frac{a_l a_{l'} a_p^* a_{p'}^* \mu_{\mathbf{y},\boldsymbol{\upsilon},\mathbf{x}_i^l}\mu_{\mathbf{y},\boldsymbol{\upsilon},\mathbf{x}_i^{l'}}(\gamma_{\mathbf{y},\boldsymbol{\upsilon}}^{ij,\beta})^2(\gamma_{\mathbf{y},\boldsymbol{\upsilon}}^{ij,\beta'})^2}{(4\pi)^4|\mathbf{y}-\mathbf{x}_j^p||\mathbf{y}-\mathbf{x}_i^l||\mathbf{y}-\mathbf{x}_j^{p'}||\mathbf{y}-\mathbf{x}_i^{l'}|}C_{p'',\nu}^{j,q}C_{p''',\nu'}^{j,q'}, \qquad (78)$$

$C_{0,0}^{ij,q,q}$ and $C_{\Gamma,\Gamma}^{ij,q,q}$ are given by (78) for $\Gamma=\Gamma'=0$ and $\Gamma=\Gamma'\neq 0$, respectively; $C_{p'',\nu}^{j,q}$ and $C_{p''',\nu'}^{j,q'}$ are as defined in (56); $\gamma_{\mathbf{y},\boldsymbol{\upsilon}}^{ij,0}$ is given by $\gamma_{\mathbf{y},\boldsymbol{\upsilon}}^{ij,\beta}$ for $\beta=(0,0)$ and Φ is given by (54). Note that the subscript or superscript 0 denotes the direct-path propagation case.

Note that the first summation in (77) corresponding to $\Gamma=\Gamma'=0$ is the SNR_λ^2 of the true target image due to the direct-path propagation; the second summation corresponding to $\Gamma=\Gamma'\neq 0$, where $p=p''$ is the SNR_λ^2 of the true target image due to the multipath propagation, and the third summation corresponding to $\Gamma\neq\Gamma'$ is the SNR_λ^2 of the artifacts in the reconstructed image.

When there are only two receivers and a single transmitter in the scene, i.e. $i=2$, $j=1$ and $q=1$, the first two summations in (77) show that the SNR_λ^2 of the true target image in a multiple-scattering environment increases by roughly a factor of $(L+1)^3$, where L is the number of the multipath bounces as compared to the image obtained with two receivers and a single transmitter in free space. However, there are also additional artifacts in the image as shown by the third summation in (77). The number of the summands in the third summation with $i=2$, $j=1$ and $q=1$ is roughly $[L(L+1)/2]^4$.

For each additional receiver, (77) shows that the SNR_λ^2 of the true target image increases by

$$C_{0,0}^{ij,q,q}\int \overline{S}_i^{-1}(\omega)\omega^4\left|\hat{p}_q\left(\frac{\gamma_{\mathbf{y},\boldsymbol{\upsilon}}^{ij,0}\,\omega}{\alpha_{0,0}^{j,q}}\right)\right|^2 \mathrm{d}\omega+\sum_{\kappa=\kappa'\neq 0}^{L} C_{\Gamma,\Gamma}^{ij,q,q}\int \overline{S}_i^{-1}(\omega)\omega^4\left|\hat{p}_q\left(\frac{\gamma_{\mathbf{y},\boldsymbol{\upsilon}}^{ij,\beta}\,\omega}{\alpha_{p,\nu}^{j,q}}\right)\right|^2 \mathrm{d}\omega \qquad (79)$$

as compared to the SNR_λ^2 for the two-receiver and a single-transmitter case. However, the number of summands in the SNR_λ^2 of the artifact component also increases roughly by a factor of $(N-1)$.

For M transmitters, SNR_λ^2 of the true target image increases by roughly a factor of M as compared to the single-transmitter case. However, as for the SNR_λ^2 of the artifact component, the number of summands in the SNR_λ^2 increases roughly by a factor of $M(M+1)/2$.

Note that although the number of summands in the SNR_λ^2 of the artifact component is much larger than that of the true target image, their strength is relatively low, because each summand in the third term is an incoherent (delayed) summation of the cross-correlation and auto-correlation of the transmitted waveforms due to the phase term in the summation. This observation is also demonstrated in our numerical simulations in the following section.

6. Numerical simulations

6.1. Simulation parameters and performance evaluation

We conducted numerical simulations to verify the theory and to demonstrate the performance of our passive imaging method using both a point target and an extended target model. For point target model, we considered scenarios containing a single and two moving point targets.

For the multiple-scattering environment, we considered two models: (i) background environment containing a single specular reflecting wall. Thus, the Green function of the background environment was modeled with the shoot-and-bounce model with one multipath bounce. (ii) Background environment containing two specular reflecting walls. In this case, the measurements included second-order reflections from the specular walls. We used this model to investigate the performance of our imaging method when there was a mismatch between the model used in image formation and the one used in synthesizing the measurements.

We conducted the simulations with different number of receivers and transmitters and different types of waveforms.

For the point target simulations, we set W_s to a single pixel and for the extended target simulations, to a 7×7 pixel window. We set W_v to a single pixel window for both the point target and extended target cases.

We synthesized the measurements using (2) under Born approximation.

We simulated the measurement noise as an additive white Gaussian process and set the SNR to 15 dB.

6.1.1. Waveforms of opportunity. Taking into account the types of waveforms available in practice as illuminators of opportunity, we used two types of transmitted waveforms in our simulations. The first type of waveform, which we refer to as high-Doppler-resolution waveforms, has high Doppler resolution and relatively poor range resolution, such as the frequency-modulated (FM) radio and television signals, the waveforms used by global system for mobile communication (GSM), etc. We simulated a high-Doppler-resolution waveform as a single-frequency continuous wave (CW) with 4 GHz carrier frequency and 0.1 s duration in our experiments. Such a waveform provides a radial-velocity resolution of about $0.375\ \mathrm{m\,s^{-1}}$ in monostatic operations. The second type of waveform, which we refer to as high-Doppler- and good-range-resolution waveforms, has not only good Doppler resolution, but also acceptable range resolution. Examples of such waveforms include wireless network (or WiFi) signals, digital video broadcasting terrestrial (DVB-T) signals and WiMAX [50] waveforms which have relatively large bandwidth that can offer reasonable range resolution. We simulated a high-Doppler and good-range resolution waveforms with the same carrier frequency and duration as the high-Doppler-resolution waveform, but with an additional frequency modulation, which results in a bandwidth of 7.5 MHz. Such a waveform provides about 19.5 m range resolution and $0.375\ \mathrm{m\,s^{-1}}$ radial-velocity resolution in monostatic operations.

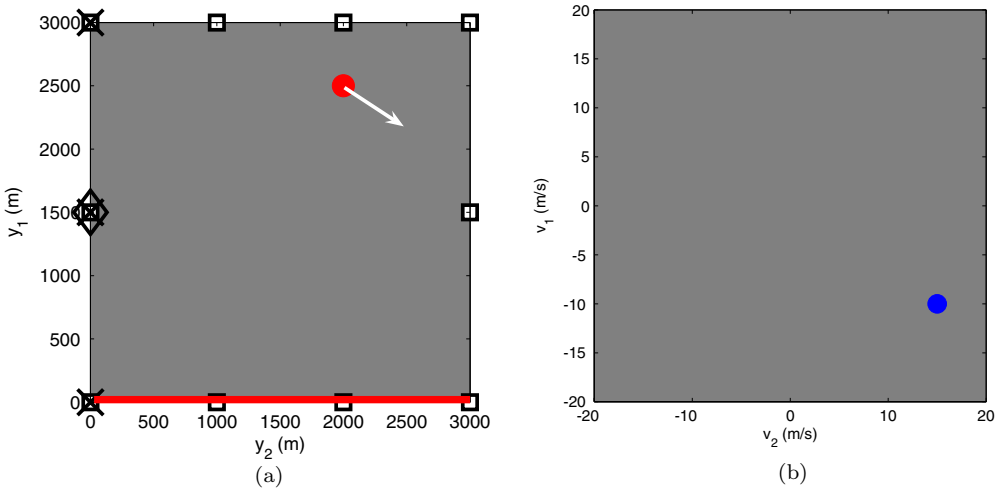

Figure 4. The 2D view of the simulation set-up. (a) Scene settings for three and ten receivers and a single transmitter. The gray region denotes the scene considered in all the numerical simulations. The red dot indicates the location of the point target with the arrow denoting the direction of the target velocity. The cross signs along the x-axis show the location of the receivers for the three-receiver case, while the blank squares show the location of the receivers for the ten-receiver case. The diamond indicates the location of the transmitter for the single-transmitter case. The reflecting wall is indicated by the solid red line at $y_1 = 0$. (b) Velocity field for a moving point target where the target velocity is indicated by the blue dot.

6.1.2. Position and velocity parameters and the number and location of receivers and transmitters. We considered a scene of size $[0, 3\times10^3]\times[0, 3\times10^3]\,\mathrm{m}^2$ with flat topography. We discretized the scene into 201×201 pixels where $[0, 0, 0]$ m and $[3 \times 10^3, 3 \times 10^3, 0]$ m correspond to the pixels $(1, 1)$ and $(201, 201)$, respectively. We assumed that the target velocity was in the range of $[-20, 20] \times [-20, 20]\,\mathrm{m\,s^{-1}}$ and discretized the velocity plane into 401×401 pixels, where $[-20, -20, 0]$ m and $[20, 20, 0]$ m correspond to the pixels at $(1, 1)$ and $(401, 401)$, respectively.

For the background environment containing a single reflecting wall, the wall was assumed to be located at $y_1 = 0$. In the single moving point target case, the target with reflectivity 2 was assumed to be located at $[2.5 \times 10^3, \quad 2 \times 10^3, \quad 0]$ m moving with velocity $[-10, 15]\,\mathrm{m\,s^{-1}}$. In the two moving point target case, an additional target with unit reflectivity was assumed to be located at $[1 \times 10^3, \quad 1.5 \times 10^3, \quad 0]$ m moving with velocity $[-10, -7]\,\mathrm{m\,s^{-1}}$. In the extended target case, the target was a square of size $90 \times 90\,\mathrm{m}^2$, which consists of a 7×7 pixel target centered at $[2.5 \times 10^3, \quad 2 \times 10^3, \quad 0]$ m with the uniform reflectivity of 1 moving with velocity $[-10, 15]\,\mathrm{m\,s^{-1}}$.

For each waveform, we performed the image reconstruction using (i) one transmitter and three receivers, (ii) one transmitter and ten receivers around the scene and (iii) two transmitters and ten receivers. In the single-transmitter case, the transmitter was assumed to be located at $[1.5 \times 10^3, 0, 6]$ m, while in the two-transmitter case, the transmitters were assumed to be located at $[1 \times 10^3, 0, 6]$ m and $[2 \times 10^3, 0, 6]$ m. Both the transmitter and receivers were assumed to be on the same plane, $y_3 = 6$ m. The receivers were assumed to lie on the y_1-axis, equidistant form each other in the range of $[0, 3 \times 10^3]$ m for the three-receiver case. For the ten-receiver case, the receivers were distributed in equal distance around the scene. Figure 4 shows the simulation set-up with a single reflecting wall and one point target. Figure 4(a) shows the location of the moving point target, the transmitter and the receivers. Figure 4(b) shows the velocity of the moving target in the velocity field.

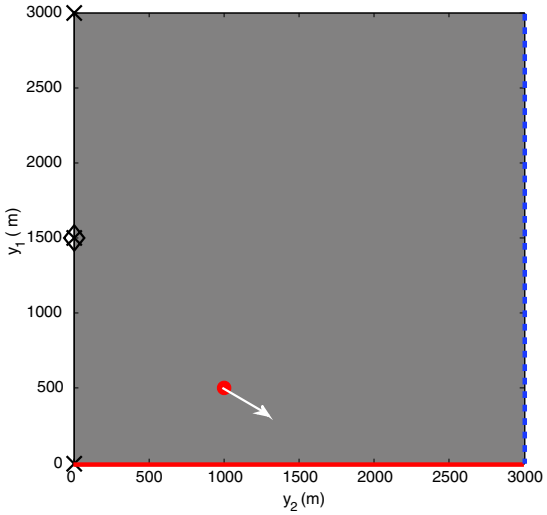

Figure 5. The 2D view of the simulation set-up for the environment model containing two reflecting walls. The two reflecting walls, as indicated by the solid red line and dashed blue line wall, are located at $y_1 = 0$ and $y_2 = 3000$ m, respectively. The target is located at $[0.5 \times 10^3, 1 \times 10^3, 0]^T$ m at time $t = 0$ moving with velocity $[-10, 15, 0]$ m s^{-1}. There are three receivers and one transmitter present in the scene. Note that the markers for the transmitter, receivers, etc, are the same as those in figure 4(a).

For the environment containing two reflecting walls, the walls were assumed to be located at $y_1 = 0$ and $y_2 = 3000$ m. The point target with unit reflectivity was assumed to be located at $[0.5 \times 10^3, \quad 1 \times 10^3, \quad 0]$ m moving with velocity $[-10, 15]$ m s^{-1}. A high-Doppler-resolution waveform was used in the experiments. Only the single transmitter and three-receiver case was considered. Figure 5 shows the simulation set-up with the two reflecting walls.

6.1.3. Image formation. We reconstructed the four-dimensional test-statistic image in $(\boldsymbol{y}, \boldsymbol{v})$ coordinates. Similar to the image formation method described in [32], we generated three two-dimensional images from the original four-dimensional image. The first image is the *peak-value image*, which was generated by choosing the maximum value of the four-dimensional image for each velocity (v_1, v_2). We then chose the maximum value, $\tilde{\boldsymbol{v}}$, of the peak-value image as the estimate of the velocity. The second image is the *position image*, which is the cross-section of the four-dimensional image, for $\boldsymbol{v} = \tilde{\boldsymbol{v}}$. We take the maximum value, $\tilde{\boldsymbol{y}}$, of the position image as an estimate of the target's position. The third image is the *velocity image*, which is the cross-section of the four-dimensional image, for $\boldsymbol{y} = \tilde{\boldsymbol{y}}$. Once the target with the largest reflectivity and its corresponding velocity is identified, we can identify the target that has the second largest reflectivity by iteratively forming the peak-value image corresponding to second largest value of the four-dimensional image for each velocity, and the corresponding position and velocity images.

6.2. Results for environment containing a single reflecting wall

6.2.1. Results using the high-Doppler-resolution waveform. Figures 6–8 show the reconstructed images using the high-Doppler-resolution waveform described in section 6.1.1 corresponding to the three different scenarios described above.

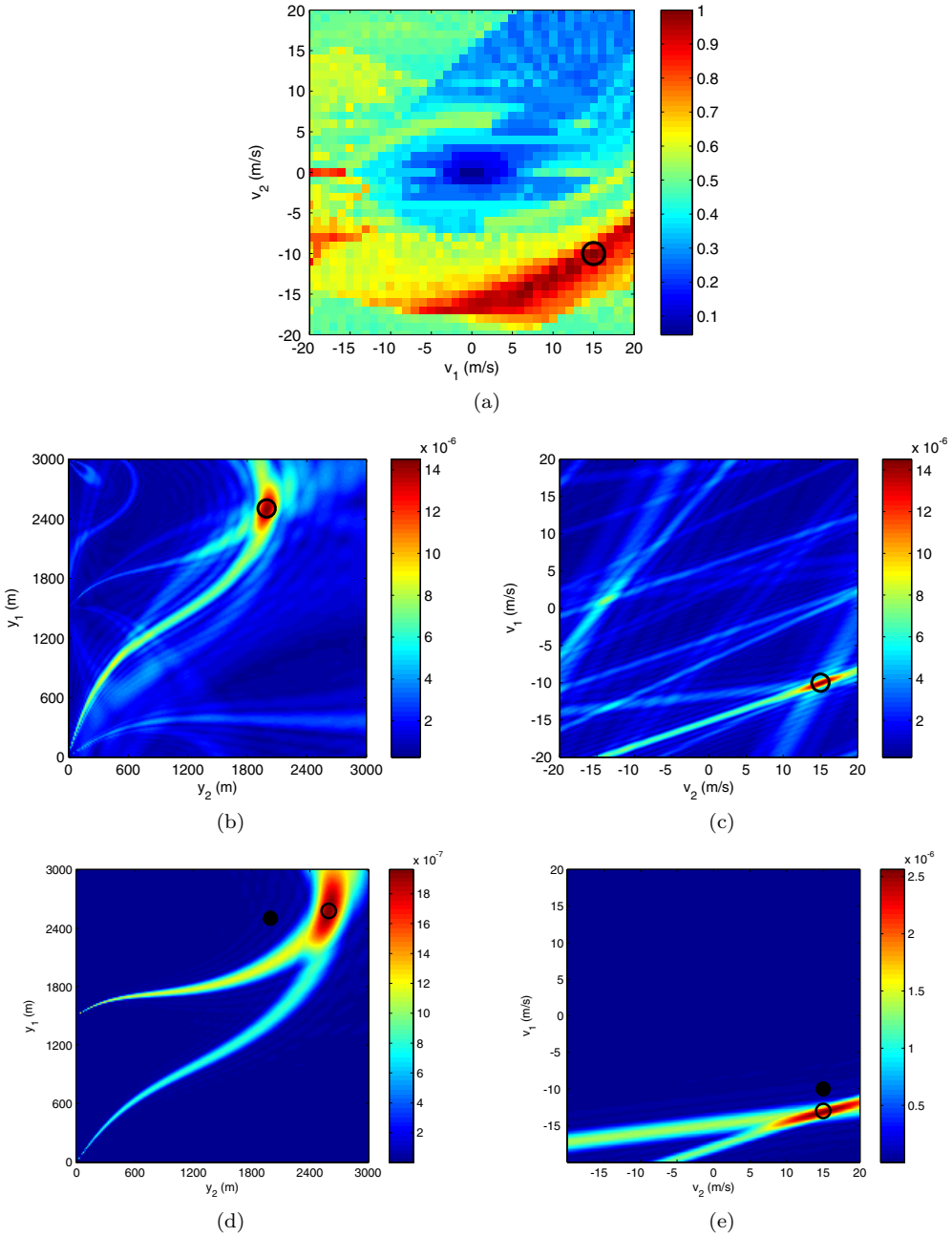

Figure 6. The reconstructed images for a moving point target using three receivers and a single transmitter transmitting a high-Doppler-resolution waveform. (a) The peak-value image with the maximum value indicated by a circle. The estimated velocity $\tilde{\boldsymbol{v}} = (-10, 15)\,\mathrm{m\,s^{-1}}$. (b) The position image when $\boldsymbol{v} = \tilde{\boldsymbol{v}}$. The estimated position $\tilde{\boldsymbol{y}} = (2500, 2000)\,\mathrm{m}$. (c) The velocity image when $\boldsymbol{y} = \tilde{\boldsymbol{y}}$. (d) The position image reconstructed using the free-space propagation model and $\tilde{\boldsymbol{v}} = (-13, 15)\,\mathrm{m\,s^{-1}}$. The estimated position $\tilde{\boldsymbol{y}} = (2580, 2595)\mathrm{m}$. (e) The velocity image reconstructed using the free-space propagation model when $\boldsymbol{y} = \tilde{\boldsymbol{y}}$. Solid dots indicate the true position (or velocity) and circles indicate the estimated position (or velocity).

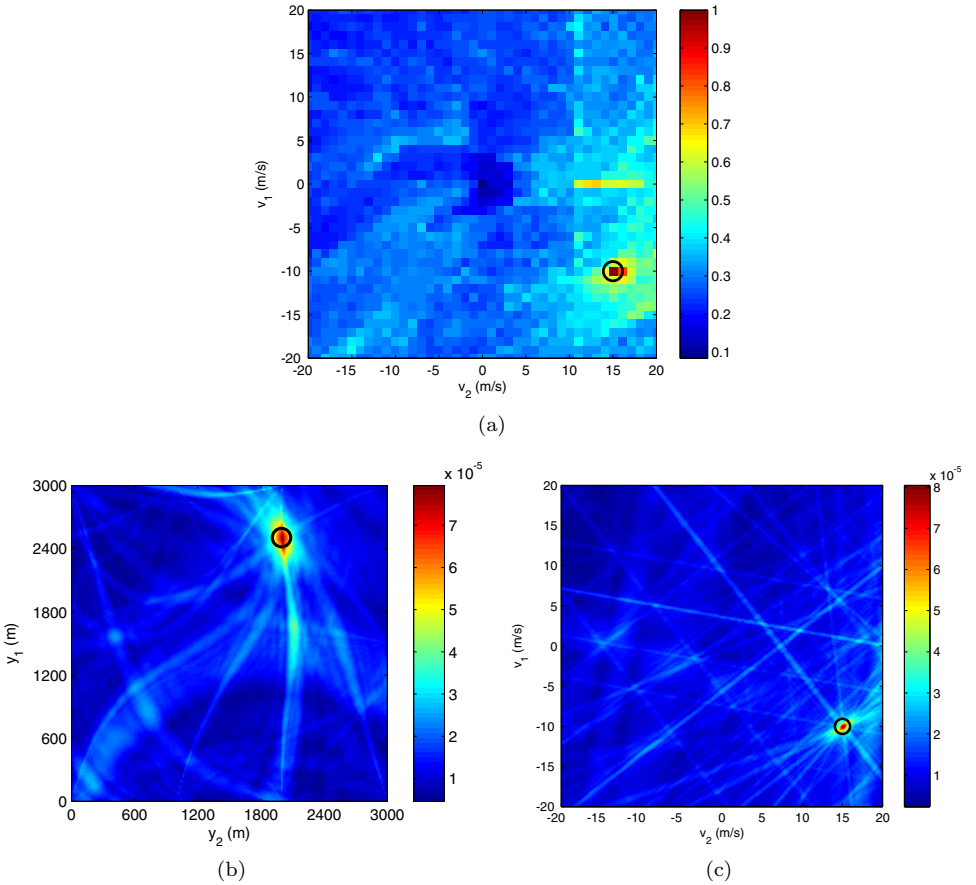

Figure 7. The reconstructed images for a moving point target using ten receivers and a single transmitter transmitting a high-Doppler-resolution waveform. (a) The peak-value image with the maximum value indicated by a circle. The estimated velocity $\tilde{\boldsymbol{v}} = (-10, 15)\,\mathrm{m\,s^{-1}}$. (b) The position image when $\boldsymbol{v} = \tilde{\boldsymbol{v}}$. The estimated position $\tilde{\boldsymbol{y}} = (2500, 2000)$ m. (c) The velocity image when $\boldsymbol{y} = \tilde{\boldsymbol{y}}$. Solid dots indicate the true position (or velocity) and circles indicate the estimated position (or velocity).

Figures 6(a), 7(a) and 8(a) show the peak-value images. The maximum value of the peak-value image, which corresponds to the estimated velocity, $\tilde{\boldsymbol{v}}$, is indicated by a black circle. Figures 6(b), 7(b) and 8(b) show the corresponding position images (cross-section of the four-dimensional image) when $\boldsymbol{v} = \tilde{\boldsymbol{v}}$. The maximum value of the position image, which corresponds to the estimated position, $\tilde{\boldsymbol{y}}$, is indicated by a black circle. For ease of comparison, the true position of the target is indicated by a black dot. Figures 6(c), 7(c) and 8(c) show the corresponding velocity images (cross-section of the four-dimensional image) when $\boldsymbol{y} = \tilde{\boldsymbol{y}}$. The maximum value of the velocity image, i.e. the estimated velocity, is indicated by a black circle. The true velocity is indicated by a black dot. Note that if the estimated value is almost equal to the true value, only the marker for the estimated value is shown.

For the purpose of comparison, the reconstructed position and velocity images for the free space using a single transmitter and three receivers are shown in figures 6(d) and (e).

Figures 9 and 10 show the vertical and horizontal profiles of the reconstructed position and velocity images of the three cases and the first case operating in free space. We also listed the 3 dB mainlobe width of the vertical and horizontal profiles in table 1 to quantitatively

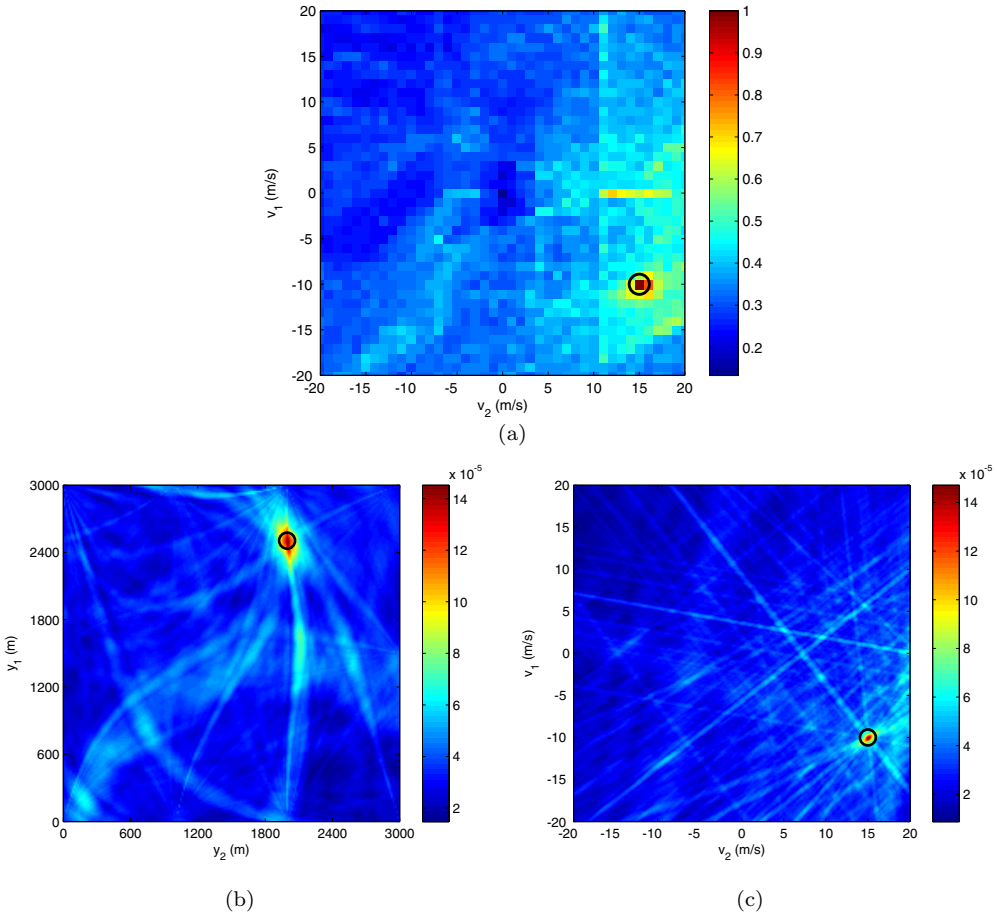

Figure 8. The reconstructed images for a moving point target using ten receivers and two transmitters transmitting a high-Doppler-resolution waveform. (a) The peak-value image with the maximum value indicated by a circle. The estimated velocity $\tilde{\boldsymbol{v}} = (-10, 15)\,\mathrm{m\,s^{-1}}$. (b) The position image when $\boldsymbol{v} = \tilde{\boldsymbol{v}}$. The estimated position $\tilde{\boldsymbol{y}} = (2500, 2000)$ m. (c) The velocity image when $\boldsymbol{y} = \tilde{\boldsymbol{y}}$. Solid dots indicate the true position (or velocity) and circles indicate the estimated position (or velocity).

Table 1. 3 dB mainlobe width of the reconstructed images using the high-Doppler-resolution waveform.

	Position image		Velocity image	
Cases	V (m)	H (m)	V ($\mathrm{m\,s^{-1}}$)	H ($\mathrm{m\,s^{-1}}$)
Three receivers, one transmitter, free space	660	229.5	1.24	5.45
(i) Three receivers, one transmitter	346.5	166.5	0.8	1.96
(ii) Ten receivers, one transmitter	249	111.75	0.71	0.765
(iii) Ten receivers, two transmitters	243	108.75	0.7	0.745

V: vertical direction.
H: horizonal direction.

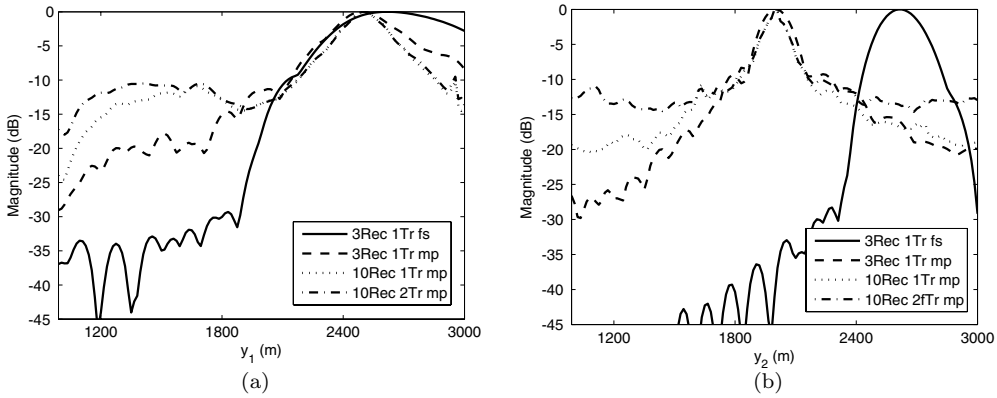

Figure 9. (a) Vertical and (b) horizontal profiles of the reconstructed position-image of the moving point target using the high-Doppler-resolution waveform.

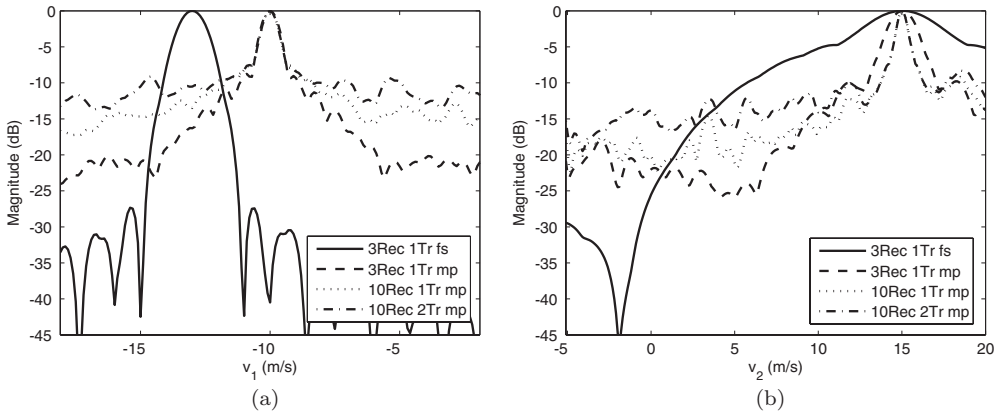

Figure 10. (a) Vertical and (b) horizontal profiles of the reconstructed velocity image of the moving point target using the high-Doppler-resolution waveform.

show the resolution improvements, where the 3 dB mainlobe width is used as a measure of resolution.

Visual comparison of figures 6(b) and (c) with figures 6(d) and (e) shows that the resolution of the position and velocity images reconstructed exploiting multiple scattering is better than the resolution of the images reconstructed using the free-space direct path only. Furthermore, the strength of the reconstructed target images is higher than that of the free-space images, which indicates that the multipath propagation improves the image contrast as shown in section 5. These visual observations are further confirmed by the vertical and horizontal profiles of the reconstructed images shown in figures 9 and 10 and the 3 dB mainlobe width listed in table 1.

We also note that additional artifacts arise in the background of the reconstructed images, as shown in figures 6(b) and (c). This is also indicated by the increase in the level of the sidelobes of the vertical and horizontal profiles for these two cases as shown in figures 9 and 10.

Table 2. 3 dB mainlobe width of the reconstructed images using the high-Doppler and good-range-resolution waveforms.

	Position image		Velocity image	
Cases	V (m)	H (m)	V ($m\,s^{-1}$)	H ($m\,s^{-1}$)
Three receivers, one transmitter, free space	64.5	411	0.995	4.05
(i) Three receivers, one transmitter	34.5	155.25	0.64	1.89
(ii) Ten receivers, one transmitter	37.5	66.75	0.7325	0.68
(iii) Ten receivers, two transmitters	36.5	53.25	0.7	0.61

V: vertical direction.
H: horizontal direction.

When the number of the receivers increases, additional position- and velocity-related passive-iso-Doppler contours intersect at the correct target position and velocity, resulting in increased test-statistic values and thus, improved position and velocity resolution as shown in figures 7(b) and (c). We can also see the resolution improvement due to the increased number of the receivers by comparing the vertical and horizontal profiles shown in figures 9 and 10 and observing the decrease in the 3 dB mainlobe width as shown in table 1.

Note that there are more artifacts arising in figures 7(b) and (c) as compared to figures 6(b) and (c), which is also indicated by the increase in the sidelobe levels in the vertical and horizontal profiles as shown in figures 9 and 10. This is consistent with our analysis in section 5 that the artifact components increase with the increasing number of receivers.

Comparing figures 8(b) and (c) with figures 7(b) and (c), we see that the test-statistic value at the correct target location and correct target velocity, and the strength of the artifacts increase as expected when an additional transmitter is added to the scene. Furthermore, more artifacts arise due to the cross-correlation of the transmitted waveforms resulting in an increase in the sidelobe levels of the vertical and horizontal profiles as shown in figures 9 and 10. As in table 1, the resolution improves moderately with the use of an additional transmitter, although this improvement is not evident visually in the reconstructed images.

Figure 11 shows the reconstructed images for two moving targets using a high-Doppler-resolution waveform. We see that our method is able to reconstruct the positions and velocities of multiple moving targets.

Figure 12 shows the reconstructed images for an extended target using a high-Doppler-resolution waveform. The image shows that our method reconstructs the extended moving target at the correct location and estimates its velocity with good accuracy. Note that the refined velocity estimation, $\tilde{\boldsymbol{v}}'$, differs from the true one, nevertheless, it is sufficiently accurate for practical applications.

6.2.2. Results using the high-Doppler- and good-range-resolution waveforms. We conducted numerical simulations using the high-Doppler and good-range-resolution waveform for the three scenarios described in subsection 6.2.1. We present the reconstructed images using ten receivers and two transmitters in figure 13. As shown in these images, the moving target is reconstructed at the correct velocity and at the correct position. The 3 dB mainlobe width of the vertical and horizontal profiles of the reconstructed images for the three scenarios is listed in table 2.

Conclusions similar to those in subsection 6.2.1 can be drawn for the image formation using a high-Doppler-resolution and good-range-resolution waveforms. The moving target is reconstructed at the correct velocity and position or with much smaller error than that of the free-space case. Both the position and velocity resolutions of the reconstructed image improve

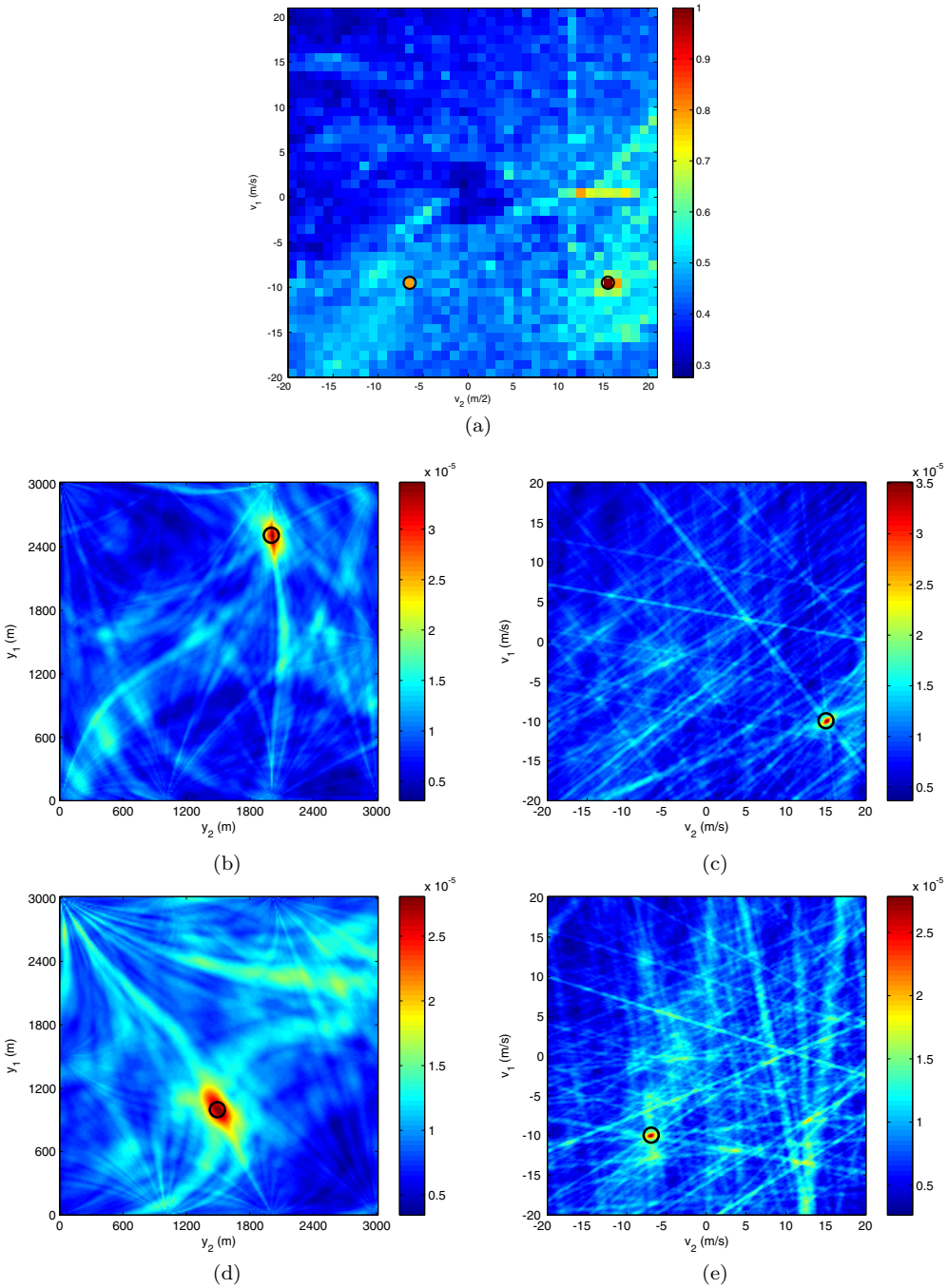

Figure 11. Reconstructed images for two moving targets using ten receivers and a single transmitter transmitting a high-Doppler-resolution waveform. (a) The peak-value image with the first two largest values marked by circles. The two estimated velocities are $\tilde{\boldsymbol{v}}_1 = [-10, 15]\,\mathrm{m\,s^{-1}}$ and $\tilde{\boldsymbol{v}}_2 = [-10, -7]\,\mathrm{m\,s^{-1}}$. (b) The position image when $\boldsymbol{v} = \tilde{\boldsymbol{v}}_1$. The estimated position $\tilde{\boldsymbol{y}}_1 = [2500, 2000]\,\mathrm{m}$. (c) The velocity image when $\boldsymbol{y} = \tilde{\boldsymbol{y}}_1$. (d) The position image when $\boldsymbol{v} = \tilde{\boldsymbol{v}}_2$. The estimated position $\tilde{\boldsymbol{y}}_2 = [1000, 1500]\,\mathrm{m}$. (e) The velocity image when $\boldsymbol{y} = \tilde{\boldsymbol{y}}_2$. The circles indicate the estimated position (or velocity).

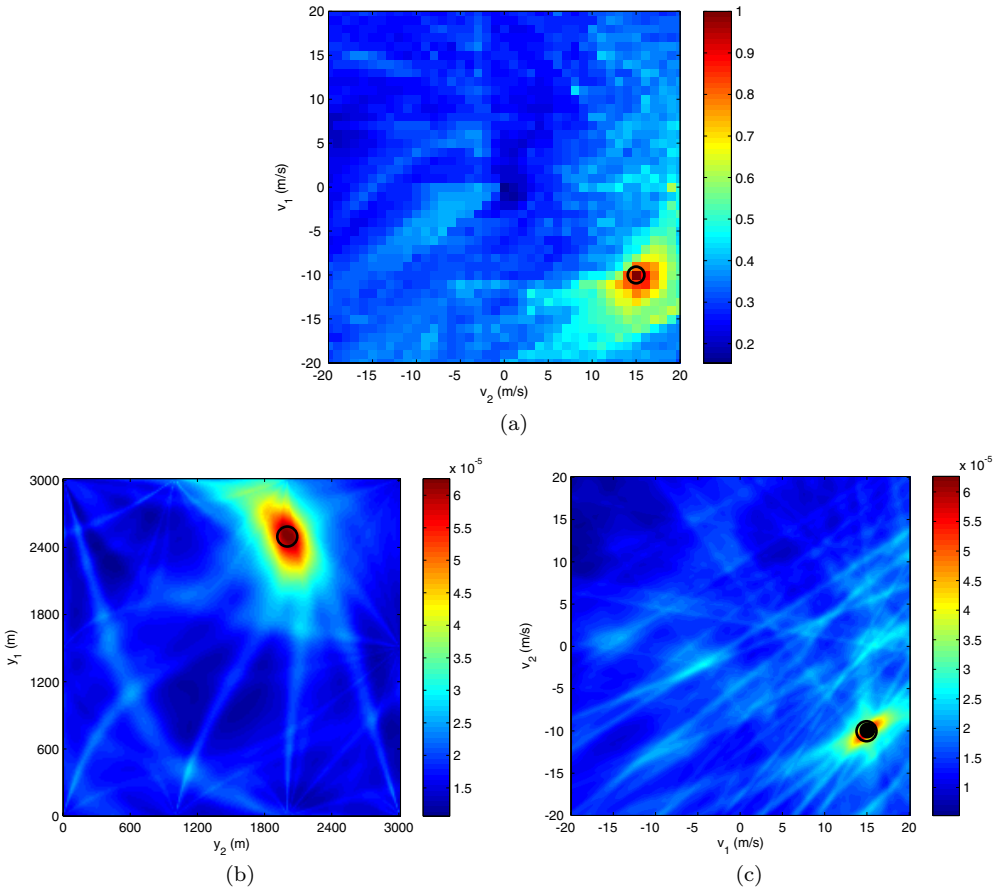

Figure 12. Reconstructed images for an extended moving target using ten receivers and a single transmitter transmitting a high-Doppler-resolution waveform. (a) The peak-value image with the largest value marked by a circle. The estimated velocity is $\tilde{\boldsymbol{v}} = [-10, 15]\,\mathrm{m\,s^{-1}}$. (b) The position image when $\boldsymbol{v} = \tilde{\boldsymbol{v}}$. The peak is located at $\tilde{\boldsymbol{y}} = [2500, 2000]\,\mathrm{m}$ marked by a circle, which is equal to the true target (center) position. (c) The velocity image when $\boldsymbol{y} = \tilde{\boldsymbol{y}}$ with the maximum value located at $\tilde{\boldsymbol{v}}' = [-10.1, 14.9]\,\mathrm{m\,s^{-1}}$, providing a refined velocity estimation.

when the multiple scattering is utilized, as well as with the increasing number of receivers and transmitters, as indicated in table 2. Likewise, the artifact components increase with the increase of the number of receivers and transmitters.

Note that the resolution improvement resulting from the increased number of transmitters is moderate as compared to the improvement resulting from the increased number of receivers when using both types of waveforms of opportunity. Additionally, our simulation results show that the reconstructed velocity images and the velocity resolution obtained using two different types of waveforms are almost the same as shown in the images in figures 13(c) and 8(c), and the 3 dB mainlobe width of the velocity profiles listed in tables 1 and 2. This is consistent with our analysis in section 5 that the velocity resolution depends only on the Doppler ambiguity of the transmitted waveforms.

We note that the position resolution obtained using the high-Doppler- and good-range resolution waveforms is better than the one obtained using the high-Doppler-resolution waveform, as shown in tables 1 and 2. These results confirm that the high-Doppler and good-

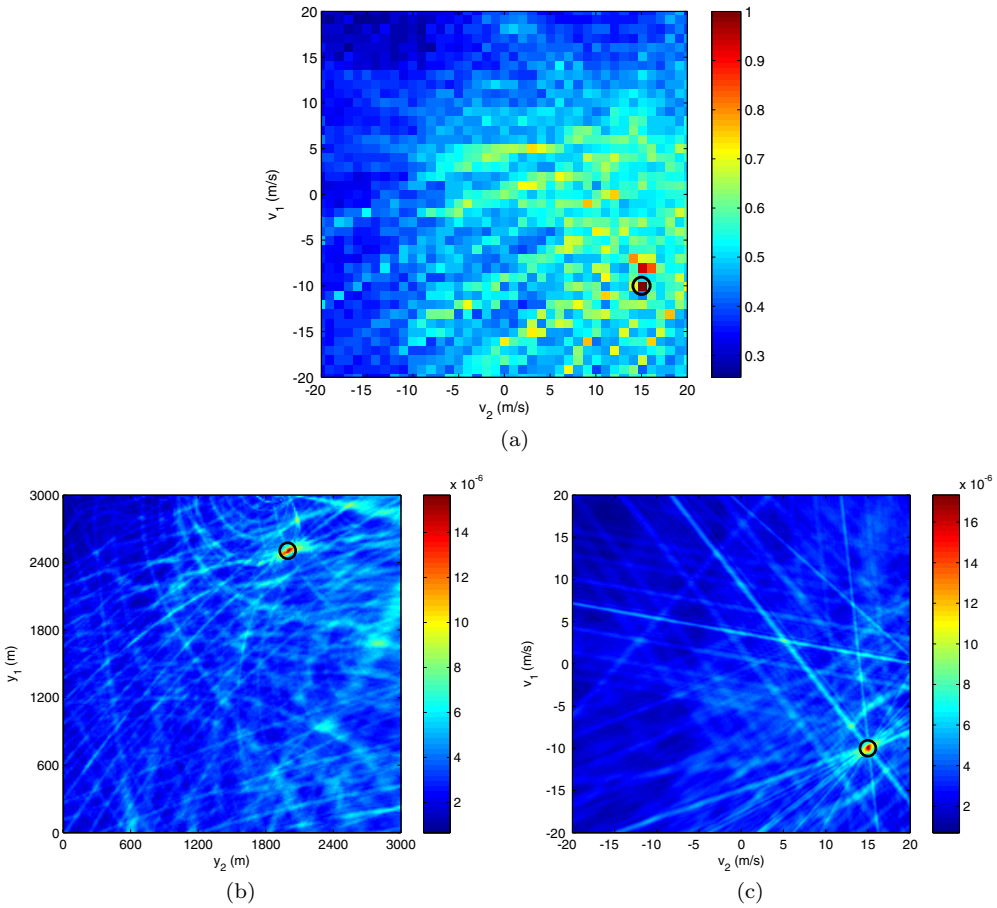

Figure 13. The reconstructed images for a moving point target using ten receivers and two transmitters transmitting a high-Doppler and good-range resolution waveforms. (a) The peak-value image with the maximum value indicated by a circle. The estimated velocity $\tilde{\boldsymbol{v}} = (-10, 15)\,\mathrm{m\,s^{-1}}$. (b) The position image when $\boldsymbol{v} = \tilde{\boldsymbol{v}}$. The estimated position $\tilde{\boldsymbol{y}} = (2500, 2000)$ m. (c) The velocity image when $\boldsymbol{y} = \tilde{\boldsymbol{y}}$. Solid dots indicate the estimated position (or velocity) and circles indicate the true target position (or velocity).

range-resolution waveform is superior to the high-Doppler-resolution waveform in position estimation.

Figure 14 shows the results for two moving targets using a high-Doppler and good-range-resolution waveforms. We see that our method can reconstruct multiple moving targets accurately in both position and velocity spaces.

Figure 15 shows the reconstructed images for an extended target using a high-Doppler- and good-range-resolution waveforms. We see that the extended target can be reconstructed in both position and velocity spaces. Note that the true target (center) position and velocity are marked by solid dots.

As shown in figures 12(b) and 15(b), the reconstructed extended target spreads to a larger area than the point target in the position space, as expected. Examining figures 12(c) and 15(c), we see that the velocity resolution in the extended target case is not as good as that of the point target case. This may be due to the interference between the multiple scatterers contained in the extended target.

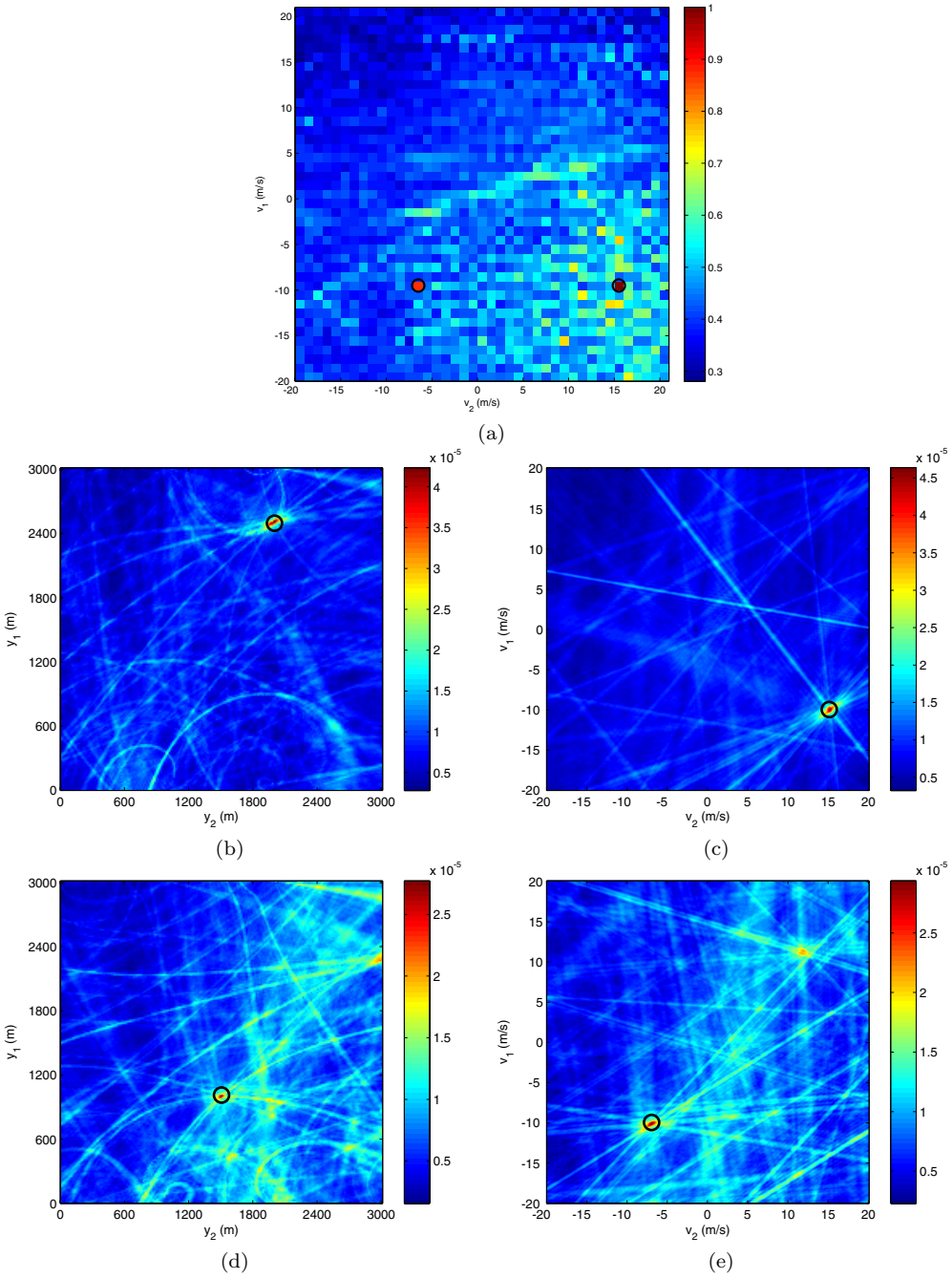

Figure 14. Reconstructed images for two moving targets using ten receivers and a single transmitter transmitting a high-Doppler-resolution and good-range-resolution waveforms. (a) The peak-value image with the first two largest values indicated by a circle. The two estimated velocities are $\tilde{\boldsymbol{v}}_1 = [-10, 15]\,\mathrm{m\,s^{-1}}$ and $\tilde{\boldsymbol{v}}_2 = [-10, -7]\,\mathrm{m\,s^{-1}}$. (b) The position image when $\boldsymbol{v} = \tilde{\boldsymbol{v}}_1$. The estimated position $\tilde{\boldsymbol{y}}_1 = [2500, 2000]\,\mathrm{m}$. (c) The velocity image when $\boldsymbol{y} = \tilde{\boldsymbol{y}}_1$. (d) The position image when $\boldsymbol{v} = \tilde{\boldsymbol{v}}_2$. The estimated position $\tilde{\boldsymbol{y}}_2 = [1000, 1500]\,\mathrm{m}$. (e) The velocity image when $\boldsymbol{y} = \tilde{\boldsymbol{y}}_2$. The circles indicate the estimated position (or velocity).

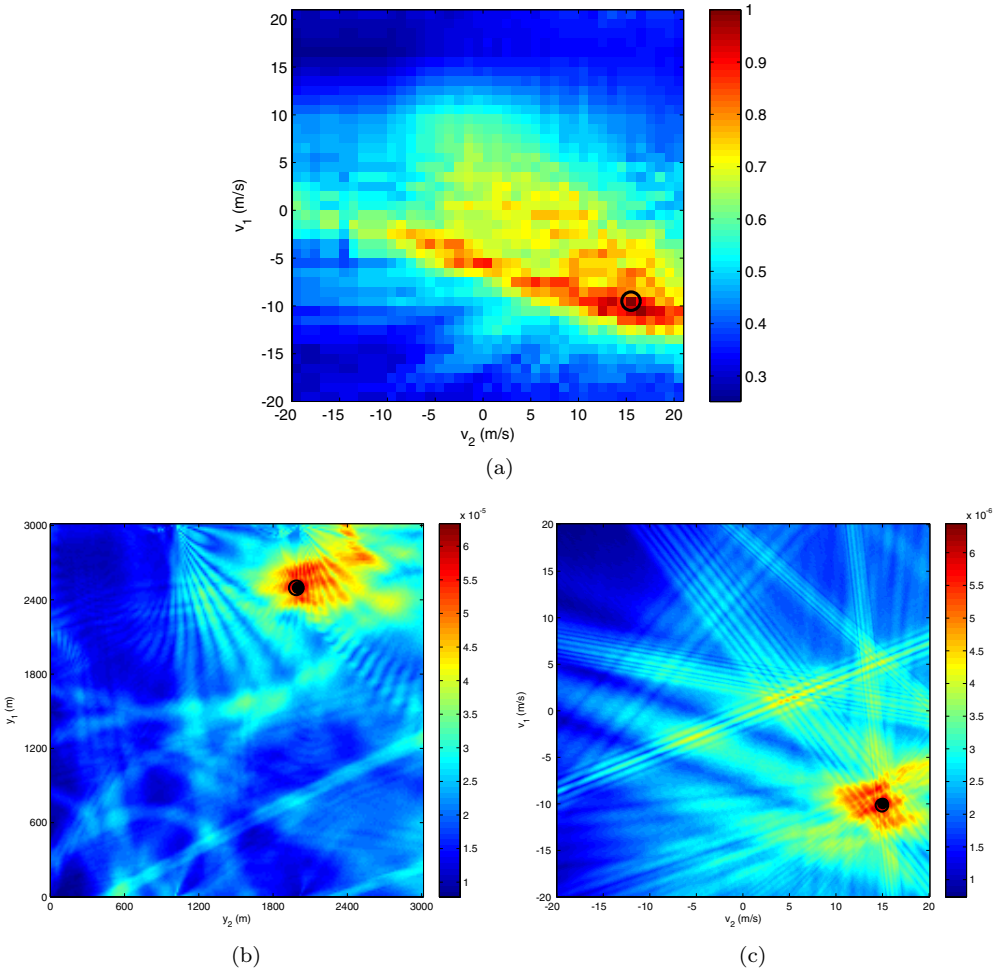

Figure 15. Reconstructed images for an extended moving target using ten receivers and a single transmitter transmitting a high-Doppler- and good-range-resolution waveforms. (a) The peak-value image with the largest value marked by a circle. The estimated velocity is $\tilde{\boldsymbol{v}} = [-10, 15]\,\mathrm{m\,s^{-1}}$. (b) The position image when $\boldsymbol{v} = \tilde{\boldsymbol{v}}$. The peak is located at $\tilde{\boldsymbol{y}} = [2490, 1980]$ m marked by a circle. The solid dot denotes the true target (center) position. (c) The velocity image when $\boldsymbol{y} = \tilde{\boldsymbol{y}}$ with the maximum value located at $\tilde{\boldsymbol{v}}' = [-10.2, 14.9]\,\mathrm{m\,s^{-1}}$, providing a refined velocity estimation.

6.3. Results with forward model mismatch

In this subsection, we present the performance of our image formation method when the measurements are synthesized with a model different than the one used in image formation. For this simulation, we assumed that there were two reflecting walls in the background environment located at $y_1 = 0$ and $y_2 = 3000$ m, as shown in figure 5. The attenuation coefficient associated with the two reflecting walls was both set to $a_l = 0.8, l = 1, 2$. The target was located at $[0.5 \times 10^3, 1 \times 10^3, 0]$ m at time $t = 0$ moving with velocity $[-10, 15, 0]\,\mathrm{m\,s^{-1}}$. There were three receivers and one transmitter present in the scene of interest, as shown in figure 5. A high-Doppler-resolution waveform was used as the source of opportunity.

We performed two sets of simulations. (i) Only the first-order specular reflections were considered in both the data generation and the image formation. (ii) The first- and second-order

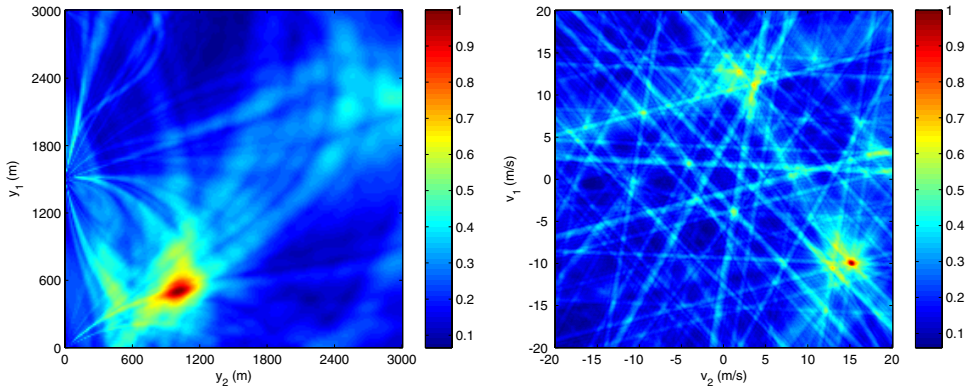

Figure 16. Reconstructed images with attenuation coefficient $a_l = 0.8, l = 1, 2$ when only the first-order reflections were considered in the received signal generation and the image formation. (a) The reconstructed position image for a fixed velocity $[-10, 15, 0]\,\mathrm{m\,s^{-1}}$ and (b) reconstructed velocity image for a fixed position $[500, 1000, 0]\,\mathrm{m}$.

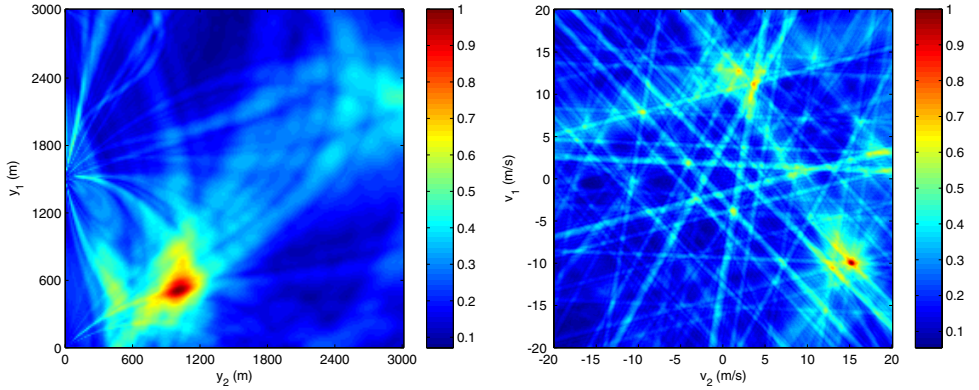

Figure 17. Reconstructed images with attenuation coefficient $a_l = 0.8, l = 1, 2$ when both the first- and second-order reflections were considered in the received signal generation, but only the first-order reflection model was used in the image formation. (a) Reconstructed position image for a fixed velocity $[-10, 15, 0]\,\mathrm{m\,s^{-1}}$ and (b) reconstructed velocity image for a fixed position $[500, 1000, 0]\,\mathrm{m}$.

specular reflections were considered in data generation, but the first-order specular reflection model was used in image formation. Figure 16 shows the reconstructed results for the first case. Figure 17 shows the reconstruction results for the second case.

We see that the reconstructed images in figure 17 are similar to those in figure 16, since the second-order specular reflections are greatly attenuated as expected.

7. Conclusions

In this paper, we presented a new passive imaging method for moving targets in position and velocity spaces using sparsely distributed receivers in multiple-scattering environments. This method is capable of exploiting the multiple scattering to improve the velocity and position estimation of targets. We developed a passive measurement model for moving targets in multiple-scattering environments. We formulated the passive image formation problem

within a GLRT framework where we set up a test of binary hypotheses using the passive measurement model for a hypothetical target located at an unknown position, moving with an unknown velocity. We designed a linear discriminant functional by maximizing the SNR of the test statistic. The passive measurement model for moving targets and the corresponding image formation method are applicable with an arbitrary Green's function model used for the multiple-scattering environments. To obtain explicit results, we used a first-order specular reflection model for the multiple-scattering environments. This model results in a discriminant functional that correlates the filtered, delayed and scaled measurements from one receiver location with the measurements at another receiver along all possible paths. The filtering is determined by the statistics of the clutter and noise. The scale is determined by the passive-Doppler-scale factor and the delay is determined by the passive range for moving targets introduced in this paper.

Our resolution analysis shows that as compared to the free-space case, the test-statistic value at the correct target location and correct target velocity increases cubically with the number of the multipath bounces in the multiple-scattering environment, linearly with the number of the receivers and transmitters. However, the multipath propagation also leads to artifacts in the reconstructed images. The strength of the artifact image depends on the number of multipath bounces, the number of receivers and transmitters and the cross-ambiguity functions of the transmitted waveforms, which is expected to be smaller than the strength of the reconstructed target due to the incoherent superposition of the auto-ambiguity and cross-ambiguity functions of the transmitted waveforms.

We presented numerical simulation results under a variety of scenarios using different transmitted waveforms of opportunity. The simulation results show that the resolution improves in the multiple-scattering environment as compared to that in free space, and improves as the number of receivers and transmitters increases.

The computational complexity of our passive moving target imaging method in multiple-scattering environment using the first-order specular reflection model is of the same order as that of passive moving target imaging in the free space [32] unless the number of background scatterers considered is very large. However, in practice our imaging method can be implemented efficiently by utilizing parallel processing and employing graphics processing units [51–53].

Note that our theoretical analysis and simulation study were carried out assuming that the measured signal consists of the scattered field only. When the measured signal includes the incident field, our method can be potentially extended to image emitters in addition to the scatterers of interest. We leave for the future the theoretical analysis and performance evaluation of this case.

Our work assumes that the Green function of the background and the statistics of the noise and clutter are known *a priori*. Our future work will focus on passive imaging exploiting multiple scattering without the knowledge about the background propagation environment and the statistics of noise and clutter.

While we mainly focused on the passive radar application, the results presented in our paper are also applicable to other wave-based passive imaging applications, such as those in acoustic or seismic imaging.

Acknowledgments

This work was supported by the Air Force Office of Scientific Research (AFOSR) under the agreements FA9550-09-1-0013 and FA9550-12-1-0415, and by the National Science Foundation (NSF) under grants CCF-08030672 and CCF-1218805.

References

[1] Griffiths H D and Baker C J 2005 Passive coherent location radar systems: part 1. Performance prediction *IEE Proc., Radar Sonar Navig.* **152** 153–9

[2] Baker C J, Griffiths H D and Papoutsis I 2005 Passive coherent location radar systems: part 2. Waveform properties *IEE Proc., Radar Sonar Navig.* **152** 160–8

[3] O'Hagan D W and Baker C J 2008 Passive bistatic radar (PBR) using FM radio illuminators of opportunity *Proc. IEEE Radar Conf. (Roma, Italy)*

[4] Howland P E, Maksimiuk D and Reitsma G 2005 FM radio based bistatic radar *IEE Proc., Radar Sonar Navig.* **152** 107–15

[5] Poullin D 2005 Passive detection using digital broadcasters (DAB, DVB) with COFDM modulation *IEE Proc., Radar Sonar Navig.* **152** 143–52

[6] Tan D K P, Sun H, Lu Y, Lesturgie M and Chan H L 2005 Passive radar using global system for mobile communication signal: theory, implementation and measurements *IEE Proc., Radar Sonar Navig.* **152** 116–23

[7] Colone F, Cardinali R and Lombardo P 2006 Cancellation of clutter and multipath in passive radar using a sequential approach *Proc. IEEE Radar Conf. (Verona, NY, USA)* pp 393–9

[8] Colone F, O'Hagan D W, Lombardo P and Baker C J 2009 A multistage processing algorithm for disturbance removal and target detection in passive bistatic radar *IEEE Trans. Aerosp. Electron. Syst.* **45** 698–722

[9] Colone F, Cardinali R, Lombardo P, Crognale O, Cosmi A, Lauri A and Bucciarelli T 2009 Space-time constant modulus algorithm for multipath removal on the reference signal exploited by passive bistatic radar *IET Radar Sonar Navig.* **3** 253–64

[10] Coleman C and Yardley H 2008 Passive bistatic radar based on target illuminations by digital audio broadcasting *IET Radar Sonar Navig.* **2** 366–75

[11] Guo H, Woodbridge K and Baker C J 2008 Evaluation of WiFi beacon transmissions for wireless based passive radar *Proc. IEEE Radar Conf. (Roma, Italy)*

[12] Chetty K, Woodbridge K, Guo H and Smith G E 2010 Passive bistatic WiMAX radar for marine surveillance *Proc. IEEE Radar Conf. (Washington, DC, USA)* pp 188–93

[13] Falcone P, Colone F, Bongioanni C and Lombardo P 2010 Experimental results for OFDM WiFi-based passive bistatic radar *Proc. IEEE Radar Conf. (Washington, DC, USA)* pp 516–21

[14] Harms H A, Davis L M and Palmer J 2010 Understanding the signal structure in DVB-T signals for passive radar detection *Proc. IEEE Radar Conf. (Washington, DC, USA)* pp 532–7

[15] Falcone P, Colone F and Lombardo P 2011 Doppler frequency sidelobes level control for WiFi-based passive bistatic radar *Proc. IEEE Radar Conf. (Kansas City, MO, USA)* pp 435–40

[16] Colone F, De Leo G, Bongioanni C and Lombardo P 2011 Direction of arrival estimation for multi-frequency FM-based passive bistatic radar *Proc. IEEE Radar Conf. (Kansas City, MO, USA)* pp 441–6

[17] Heunis S, Paichard Y and Inggs M 2011 Passive radar using a software-defined radio platform and opensource software tools *Proc. IEEE Radar Conf. (Kansas City, MO, USA)* pp 879–84

[18] He X, Cherniakov M and Zeng T 2005 Signal detectability in SS-BSAR with GNSS non-cooperative transmitter *IEE Proc., Radar Sonar Navig.* **152** 124–32

[19] Wu Y and Munson D C 2001 Multistatic synthetic aperture imaging of aircraft using reflecting television signals *Proc. SPIE* **4382** 1–12

[20] Kulpa K S 2005 Multi-static entirely passive detection of moving targets and its limitations *IEE Proc., Radar Sonar Navig.* **152** 169–73

[21] Homer J, Kubik K, Mojarrabi B, Longstaff I, Donskoi E and Cherniakov M 2002 Passive bistatic radar sensing with LEOS based transmitters *Proc. IEEE Int. Geoscience and Remote Sensing Symp. (Toronto, Canada)* pp 438–40

[22] Wang L, Son I Y and Yazıcı B 2010 Passive imaging using distributed apertures in multiple scattering environments *Inverse Problems* **26** 065002

[23] Yarman C E and Yazıcı B 2008 Synthetic aperture hitchhiker imaging *IEEE Trans. Imaging Process.* **17** 2156–73

[24] Yarman C E, Wang L and Yazıcı B 2010 Doppler synthetic aperture hitchhiker imaging *Inverse Problems* **26** 065006

[25] Prickect M J and Chen C C 1980 Principles of inverse synthetic aperture radar *EASCON'80: Electronics and Aerospace Systems Conf. (Arlington, VA)* pp 340–5

[26] Norton S J and Linzer M 1987 Backprojection reconstruction of random source distributions *The J. Acoust. Soc. Am.* **81** 977–85

[27] Borcea L, Papanicolaou G and Tsogka C 2006 Coherent interferometric imaging in clutter *Geophysics* **71** 65–75

[28] Derveaux G, Papanicolaou G and Tsogka C 2007 Time reversal imaging for sensor networks with optimal compensation in time *J. Acoust. Soc. Am.* **121** 2071–85
[29] Garnier J and Papanicolaou G 2009 Passive sensor imaging using cross correlations of noisy signals in a scattering medium *SIAM J. Imaging Sci.* **2** 396–437
[30] Garnier J and Papanicolaou G 2010 Resolution analysis for imaging with noise *Inverse Problems* **26** 074001
[31] Voccola K, Yazici B, Cheney M and Ferrara M 2009 On the relationship between the generalized likelihood ratio test and backprojection method in synthetic aperture imaging *Proc. SPIE* **7335** 73350I
[32] Wang L and Yazıcı B 2012 Passive imaging of moving targets using sparse distributed apertures *SIAM J. Imaging Sci.* **5** 769–808
[33] Hayvaci H T, Maio A D and Erricolo D 2011 Diversity in receiving strategies based on time-delay analysis in the presence of multipath *Proc. IEEE Radar Conf. (Kansas City, MO, USA)* pp 1040–5
[34] Linnehan R, Deming R and Schindler J 2011 Multipath analysis of dismount radar responses *Proc. IEEE Radar Conf. (Kansas City, MO, USA)* pp 474–9
[35] Sen S and Nehorai A 2011 Adaptive OFDM radar for target detection in multipath scenarios *IEEE Trans. Signal Process.* **59** 78–90
[36] Sen S, Tang G and Nehorai A 2011 Sparsity-based estimation for target detection in multipath scenarios *Proc. IEEE Radar Conf. (Kansas City, MO, USA)* pp 303–8
[37] Cheney M 2001 A mathematical tutorial on synthetic aperture radar *SIAM Rev.* **43** 301–12
[38] Skolnik M I 2008 *Introduction to Radar Systems* 3rd edn (New York: McGraw-Hill)
[39] Monte L Lo, Parker J, Vela R and Baker C 2012 A calibration procedure for ground-based rf tomography *Proc. IEEE Radar Conf. (Baltimore, MD, USA)* pp 635–640
[40] Palmer J and Searle S 2012 Evaluation of adaptive filter algorithms for clutter cancellation in passive bistatic radar *Proc. IEEE Radar Conf. (Baltimore, MD, USA)* pp 635–40
[41] Bleistein N, Cohen J K and Stockwell J W 2001 *Mathematics of Multi-dimensional Seismic Imaging, Migration and Inversion, Interdisciplinary Applied Mathematics* (New York: Springer)
[42] Born M and Wolf E 1999 *Principles of Optics* 7th edn (New York: Cambridge University Press)
[43] Linnehan R, Deming R and Schindler J 2011 Multipath analysis of dismount radar responses *Proc. IEEE Radar Conf. (Kansas City, MO, USA)* pp 474–9
[44] Liang G and Bertoni H L 1998 A new approach to 3-d ray tracing for propagation prediction in cities *IEEE Trans. Antennas Propag.* **46** 853–63
[45] Sen S and Nehorai A 2011 Adaptive of DM radar for target detection in multipath scenarios *IEEE Trans. Signal Process.* **59** 78–90
[46] Sen S, Tang G and Nehorai A 2011 Sparsity-based estimation for target detection in multipath scenarios *Proc. IEEE Radar Conf. (Kansas City, MO, USA)* pp 303–8
[47] Li L and Krolik J L 2011 Vehicular MIMO SAR imaging in multipath environments *Proc. IEEE Radar Conf. (Kansas City, MO, USA)* pp 989–94
[48] Kay S M 1998 *Fundamentals of Statistical Signal Processing* Vol I and Vol II (Englewood Cliffs, NJ: Prentice Hall)
[49] Barrett H H and Myers K J 2003 *Foundations of Image Science* (New York: Wiley-Interscience)
[50] IEEE *IEEE Std.* 802.16e2 005 and *IEEE Std.* 802.16d2 005 *Part 16: Air Interface for Fixed and Mobile Broadband Wireless Access Systems*
[51] Tasora A, Negrut D and Anitescu M 2011 GPU-based parallel computing for the simulation of complex multibody systems with unilateral and bilateral constraints: an overview *Computational Methods in Applied Sciences: Multibody Dynamics* vol 23 (Berlin: Springer) pp 283–307
[52] Liu Y and Hu J 2011 GPU-based parallelization for fast circuit optimization *ACM Trans. Des. Autom. Electron. Syst.* **16** 943–6
[53] Capozzoli A, Curcio C and Liseno A 2012 GPU-based ω-k tomographic processing by 1d non-uniform FFTs *Prog. Electromagn. Res.* **23** 279–98